Virtual height characteristics of ionospheric and ground scatter observed by mid-latitude SuperDARN HF radars

Evan G. Thomas[1] and Simon George Shepherd[1]

[1]Dartmouth College

November 26, 2022

Abstract

Propagation of high-frequency (HF) radio signals is strongly dependent on the ionospheric electron density structure along a communications link. The ground-based, HF space weather radars of the Super Dual Auroral Radar Network (SuperDARN) utilize the ionospheric refraction of transmitted signals to monitor the global circulation of E- and F-region plasma irregularities. Previous studies have assessed the propagation characteristics of backscatter echoes from ionospheric irregularities in the auroral and polar regions of the Earth's ionosphere. By default, the geographic location of these echoes are found using empirical models which estimate the virtual backscattering height from the measured range along the radar signal path. However, the performance of these virtual height models has not yet been evaluated for mid-latitude SuperDARN radar observations or for ground scatter propagation modes. In this study, we derive a virtual height model suitable for mid-latitude SuperDARN observations using 5 years of data from the Christmas Valley East and West radars. This empirical model can be applied to both ionospheric and ground scatter observations and provides an improved estimate of the ground range to the backscatter location compared to existing high-latitude virtual height models. We also identify a region of overlapping half-hop F-region ionospheric scatter and one-hop E-region ground scatter where the measured radar parameters (e.g., velocity, spectral width, elevation angle) are insufficient to discriminate between the two scatter types. Further studies are required to determine whether these backscatter echoes of ambiguous origin are observed by other mid-latitude SuperDARN radars and their potential impact on scatter classification schemes.

Virtual height characteristics of ionospheric and ground scatter observed by mid-latitude SuperDARN HF radars

E. G. Thomas[1], S. G. Shepherd[1]

[1]Thayer School of Engineering, Dartmouth College, Hanover, New Hampshire, USA

Key Points:

- We derive a new empirical virtual height model suitable for improved geolocation of mid-latitude SuperDARN HF radar observations
- The new model provides the first characterization of ground scatter propagation modes
- Characteristics of half-hop F-region ionospheric scatter and one-hop E-region ground scatter are examined

Corresponding author: Evan G. Thomas, `evan.g.thomas@dartmouth.edu`

Abstract

Propagation of high-frequency (HF) radio signals is strongly dependent on the ionospheric electron density structure along a communications link. The ground-based, HF space weather radars of the Super Dual Auroral Radar Network (SuperDARN) utilize the ionospheric refraction of transmitted signals to monitor the global circulation of E- and F-region plasma irregularities. Previous studies have assessed the propagation characteristics of backscatter echoes from ionospheric irregularities in the auroral and polar regions of the Earth's ionosphere. By default, the geographic location of these echoes are found using empirical models which estimate the virtual backscattering height from the measured range along the radar signal path. However, the performance of these virtual height models has not yet been evaluated for mid-latitude SuperDARN radar observations or for ground scatter propagation modes. In this study, we derive a virtual height model suitable for mid-latitude SuperDARN observations using 5 years of data from the Christmas Valley East and West radars. This empirical model can be applied to both ionospheric and ground scatter observations and provides an improved estimate of the ground range to the backscatter location compared to existing high-latitude virtual height models. We also identify a region of overlapping half-hop F-region ionospheric scatter and one-hop E-region ground scatter where the measured radar parameters (e.g., velocity, spectral width, elevation angle) are insufficient to discriminate between the two scatter types. Further studies are required to determine whether these backscatter echoes of ambiguous origin are observed by other mid-latitude SuperDARN radars and their potential impact on scatter classification schemes.

1 Introduction

The ground-based, high-frequency (HF) space weather radars of the Super Dual Auroral Radar Network (SuperDARN) utilize ionospheric refraction to routinely measure the line-of-sight (LOS) Doppler velocity of backscattered signals from E- and F-region plasma irregularities out to ranges of several thousand kilometers (Greenwald et al., 1995). The ability of SuperDARN radars to monitor ionospheric plasma convection therefore depends on two conditions: the presence of decameter-scale ionospheric irregularities, and suitable propagation conditions such that the transmitted HF radio waves can achieve perpendicularity to the magnetic field-aligned irregularities to satisfy the coherent Bragg scattering condition and return to the radar (Greenwald et al., 1985).

At auroral latitudes (60°–85° magnetic latitude, or MLAT), where the first SuperDARN radars were located, both the occurrence of E- and F-region irregularities (e.g., Ruohoniemi & Greenwald, 1997; Ballatore et al., 2000; Koustov et al., 2004; Ghezelbash et al., 2014; Koustov et al., 2019; Marcucci et al., 2021) and HF propagation conditions (e.g., André et al., 1998; Yeoman et al., 2001; Gauld et al., 2002; Chisham et al., 2008; Yeoman et al., 2008; Ponomarenko et al., 2010) have been studied in great detail. More recently, new SuperDARN radars have been constructed at both mid-latitudes and in the polar cap for improved monitoring of global convection during periods of enhanced geomagnetic activity (Chisham et al., 2007; Nishitani et al., 2019). At midlatitudes, there is therefore a smaller body of work examining the irregularity and propagation characteristics (e.g., Nishitani & Ogawa, 2005; Ribeiro et al., 2012; de Larquier et al., 2013; Oinats et al., 2016; Shepherd et al., 2020; Wang et al., 2022).

It is important to note that most studies using SuperDARN data have focused on the occurrence and propagation modes of HF backscatter from ionospheric irregularities, or ionospheric scatter (IS). An important byproduct of the sky-wave propagation mode used by SuperDARN radars is the occurrence of ground scatter (GS) echoes from land and ocean surfaces along the signal path. While these GS returns are often treated as noise when producing global maps of ionospheric plasma motion (Chisham & Pinnock, 2002), they can be useful for monitoring different geophysical phenomena such as traveling ionospheric disturbances (e.g., Bristow et al., 1996; He et al., 2004; Frissell et al., 2016), HF absorption caused by solar flares (e.g., Hosokawa et al., 2000; Chakraborty et al., 2018), or even land and ocean surface features (Shand et al., 1998; Ponomarenko et al., 2010; Greenwood et al., 2011).

Many SuperDARN radars have a secondary interferometer antenna array to measure the angle of arrival, or elevation angle, of received signals. Because HF radio waves undergo refraction as they traverse electron density gradients in the ionosphere, the actual height of the IS echo (or reflection height for GS) will always be lower in altitude than for a signal traveling the same total distance along a straight-line path with the same elevation angle. Breit and Tuve (1926) demonstrated how, for a flat Earth and planar ionosphere, the propagation paths associated with these true and "virtual" heights have the same ground range. SuperDARN radars can therefore use this virtual height information to estimate the ground range to an IS or GS backscatter location as described below.

The triangular virtual height geometry of Breit and Tuve (1926) has often been adapted to describe $\frac{1}{2}$- and $1\frac{1}{2}$-hop IS propagation modes over a spherical Earth (e.g., Chisham et al., 2008; Greenwald et al., 2017). One can extend this application of the law of cosines to define a more general set of equations which describe both IS and GS propagation modes. From the measured slant range r and elevation angle α of the received radar signal, the corresponding virtual height h_N for any N-hop propagation mode (assuming a spherical Earth with radius R_E) can be found using:

$$h_N(r,\alpha) = \left[R_E^2 + \left(\frac{r}{2N}\right)^2 + \left(\frac{r}{N}\right) R_E \sin(\alpha)\right]^{\frac{1}{2}} - R_E \tag{1}$$

where integer values of N (e.g., 1, 2, 3, etc.) correspond to GS propagation modes while fractional values of N (e.g., $\frac{1}{2}$, $1\frac{1}{2}$, $2\frac{1}{2}$, etc.) correspond to IS propagation modes. Note that for the multi-hop case ($N > 1$), the virtual height is assumed to be constant for all ionospheric reflection and/or backscatter locations. The ground range G_N to each IS or GS echo for any N-hop propagation mode can then be found using:

$$G_N(r,\alpha,h_N) = 2NR_E \sin^{-1}\left[\frac{\left(\frac{r}{2N}\right)\cos(\alpha)}{R_E + h_N}\right] \tag{2}$$

Alternatively, for cases where the elevation angle is not known (e.g., when using a virtual height model) the ground range G_N can be found using:

$$G_N(r,h_N) = 2NR_E \cos^{-1}\left[\frac{R_E^2 + (R_E+h_N)^2 - \left(\frac{r}{2N}\right)^2}{2R_E(R_E+h_N)}\right] \tag{3}$$

Figure 1 illustrates sample HF propagation geometries found using Equations 1–3 for $N \leq 2$, where we have chosen input values of r and α to obtain a representative F-region virtual height of 300 km in each panel. In their consideration of the $\frac{1}{2}$-hop IS propagation mode, Greenwald et al. (2017) refer to this approach as the "two-parameter method" due to the reliance on r and α as input parameters. However, for the more general treatment of either IS or GS, it is clear that a third input parameter specifying the number of hops (i.e., N) is also required for an accurate ground range determination.

In practice, not all SuperDARN radars have a secondary interferometer array for the measurement of elevation angles, or the time delays needed to accurately calculate the elevation data (t_{diff}) have not been properly calibrated (Chisham et al., 2021). For this more common scenario, empirical models of virtual height are used for the geolocation of line-of-sight (LOS) observations. The standard SuperDARN virtual height model (hereafter referred to as the standard VHM) was derived from observations of IS measured by the original SuperDARN radar at Goose Bay (53.32° N, 60.46° W) overlooking the auroral zone of the high-latitude ionosphere (Greenwald et al., 1985, 2017). This

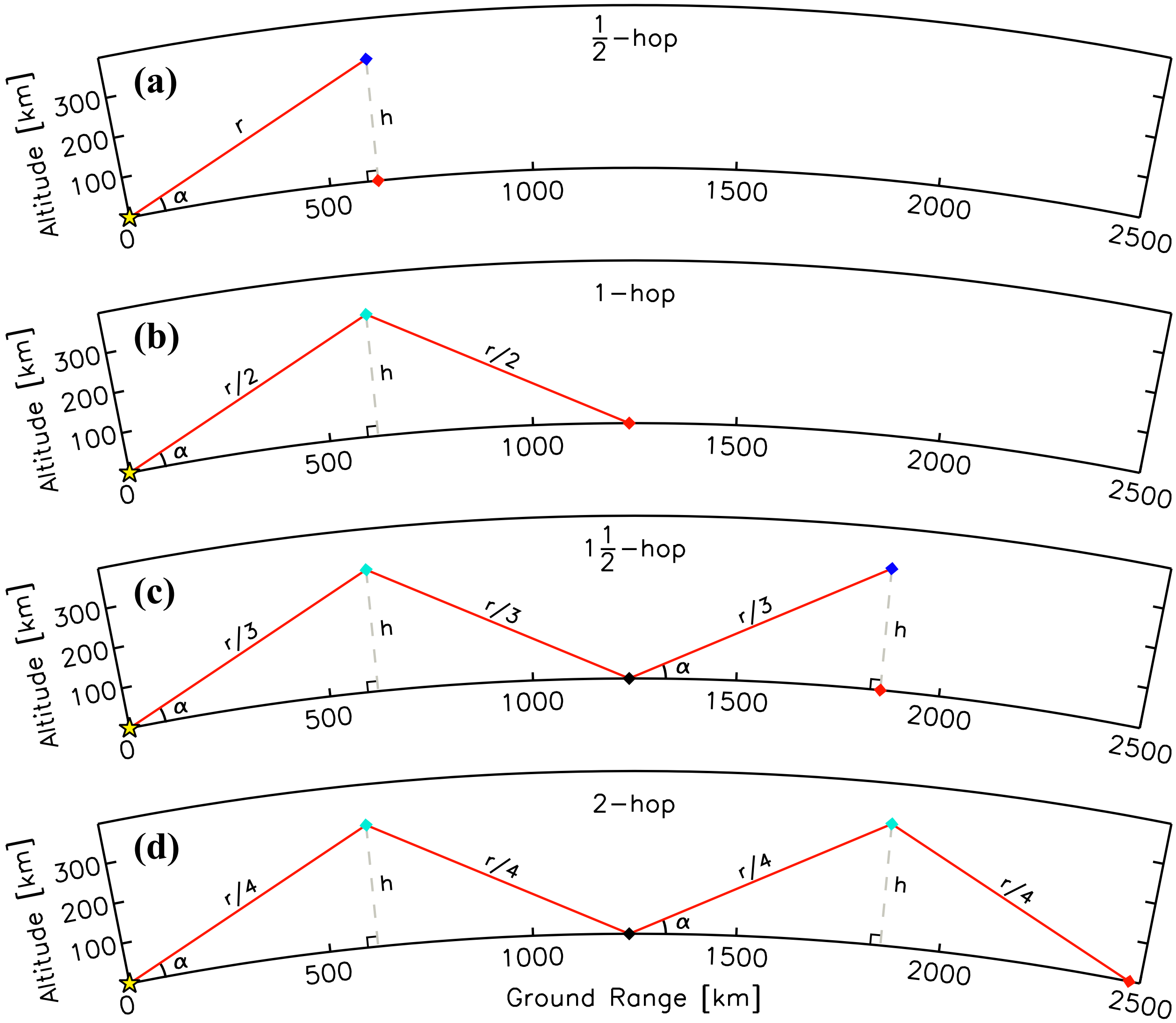

Figure 1. Illustration of (a) $\frac{1}{2}$-hop, (b) 1-hop, (c) $1\frac{1}{2}$-hop, and (d) 2-hop F-region propagation geometries as a function of slant range r, elevation angle α, and virtual height h, assuming a spherical Earth with radius R_E. Blue diamonds indicate ionospheric backscatter locations, while red diamonds indicate the ground range associated with each ionospheric or ground backscatter location. Cyan and black diamonds indicate ionospheric and ground reflection points, respectively, while the yellow star at zero ground range indicates the radar location.

model is divided into two segments, with the $\frac{1}{2}$-hop E-region and $\frac{1}{2}$-hop F-region propagation modes connected by a simple linear transition:

$$h(r) = \begin{cases} \frac{115r}{150} & 0 < r \leq 150 \text{ km} \\ 115 & 150 < r \leq 600 \text{ km} \\ \frac{r-600}{200}(h_i - 115) + 115 & 600 < r < 800 \text{ km} \\ h_i & r \geq 800 \text{ km} \end{cases} \tag{4}$$

where r is the measured slant range and h_i is the user-provided F-region virtual height (typically either 300 or 400 km). Note that SuperDARN radars usually do not record samples at ranges nearer than 180 km, although some non-standard operating modes de-

Table 1. The coefficients for Equation 5 for the Chisham et al. (2008) VHM.

Propagation Mode	A	B	C
$\frac{1}{2}$-hop E-region	108.974	0.0191271	6.68283×10^{-5}
$\frac{1}{2}$-hop F-region	384.416	-0.178640	1.81405×10^{-4}
$1\frac{1}{2}$-hop F-region	1098.28	-0.354557	9.39961×10^{-5}

signed for lower atmospheric measurements (such as mesospheric winds) may collect data at these very near ranges (e.g., Yukimatu & Tsutsumi, 2002).

More recently, Chisham et al. (2008) derived a virtual height model (hereafter referred to as the Chisham VHM) using 5 years of IS measurements from the high-latitude Saskatoon (SAS) SuperDARN radar (52.16° N, 106.53° W), fitting a low-order polynomial (or quadratic) of the form

$$h(r) = A + Br + Cr^2 \tag{5}$$

to the $\frac{1}{2}$-hop E-region, $\frac{1}{2}$-hop F-region, and $1\frac{1}{2}$-hop F-region distributions; the coefficients for each model propagation mode are listed in Table 1. It should be noted that the Chisham VHM was derived by first evaluating and then combining observations from four equally-spaced azimuthal beam directions (beams 3, 6, 9, and 12) and all local times, seasons, and radar operating frequencies. Greenwald et al. (2017) assessed the performance of the Chisham VHM using numerical ray-tracing simulations through the International Reference Ionosphere (IRI) model (Bilitza et al., 2011) at three different local times and a single frequency, finding the best agreement in terms of virtual height during nighttime conditions (∼21 LT) when the SAS radar is most likely to observe IS.

Most recently, Liu et al. (2012) derived an alternative virtual height model using ray-tracing simulations and IS observations from the high-latitude Hankasalmi radar (62.32° N, 26.61° E) to fit a quadratic of the form

$$h(r, \alpha) = Ar^2 + Br + C\alpha^2 + D\alpha + Er\alpha + F \tag{6}$$

to the $\frac{1}{2}$-hop F-region distribution (630–1980 km slant range) only. Because this model is not relevant for $\frac{1}{2}$-hop E-region or $1\frac{1}{2}$-hop F-region scatter, it is of more limited use for geolocation purposes than either the standard or Chisham VHMs. Furthermore, this model relies upon both the measured range r and elevation angle α as input, and is therefore not useful for radars without secondary interferometer arrays or calibrated t_{diff} values.

None of these virtual height models are appropriate for accurately mapping GS echoes to the Earth's surface; neither is the current implementation of Equation 1 in the SuperDARN geolocation software, which can only support the $\frac{1}{2}$-hop propagation mode. As an example, the different propagation geometries of $\frac{1}{2}$-hop IS and 1-hop GS echoes at the same measured ranges ($1000 < r < 2000$ km) are shown in Figures 2a and 2b for a spherical Earth. The cyan diamonds indicate the ionospheric reflection point of the IS or GS echoes predicted by the standard VHM (blue line), while the red diamonds indicate the associated ground range of the backscattered signals.

There is one additional factor which must be considered before comparing the ground ranges found for the IS and GS propagation modes in Figure 2. The azimuthal beam direction ϕ relative to the radar boresight is given by

$$\sin \phi = \frac{\sin \phi_0}{\cos \alpha} \tag{7}$$

where ϕ_0 is the direction at $\alpha = 0°$ (horizontal) set electronically by the radar hardware. The final ground location of the backscattering target will, therefore, vary as a function of elevation angle not only in range but also in azimuth. The latter is often ignored when determining ground range errors.

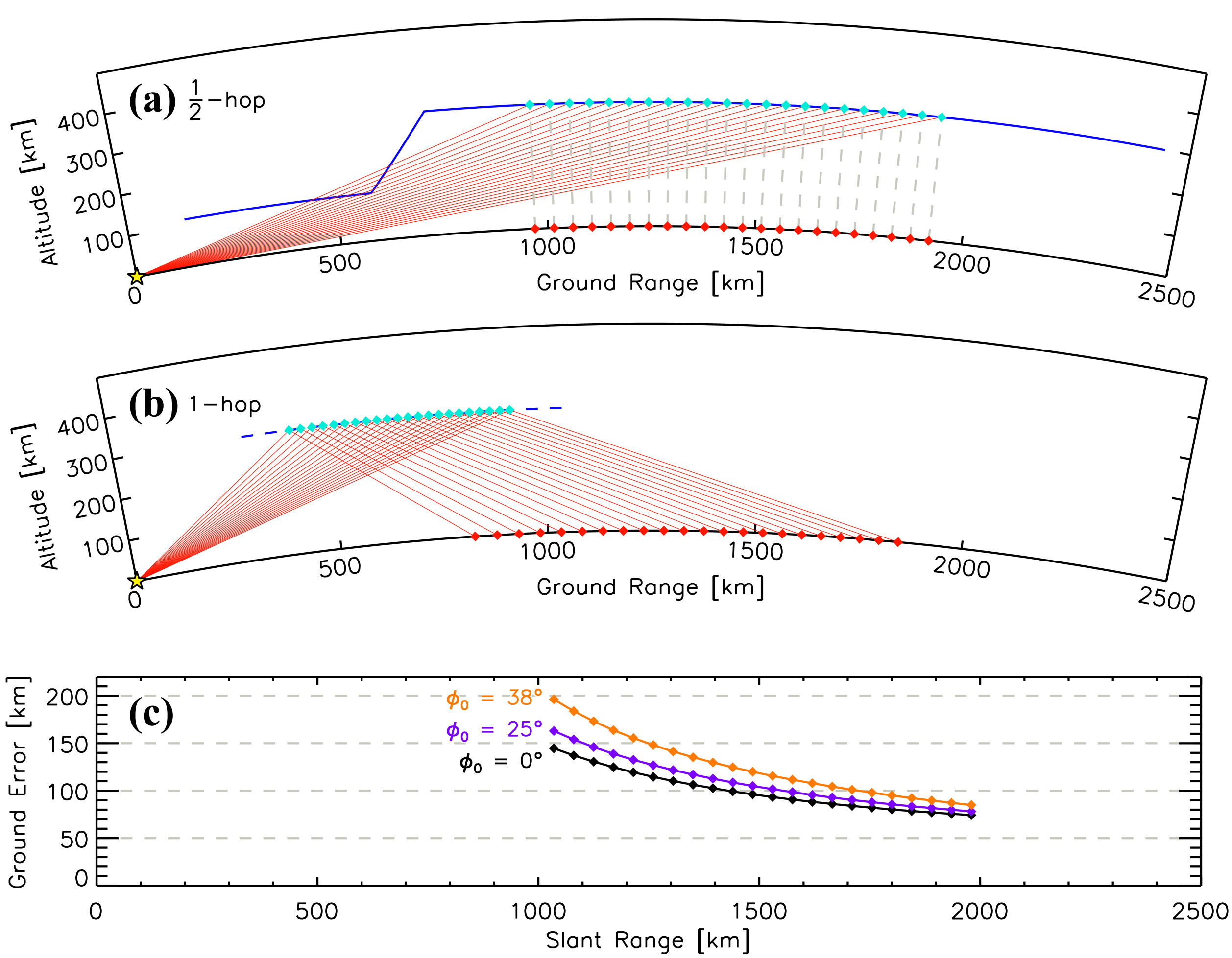

Figure 2. (a) Example of ground range mapping using the standard VHM (blue line) for measured slant ranges r between 1000–2000 km at 45 km resolution assuming a $\frac{1}{2}$-hop propagation mode (i.e., ionospheric backscatter) and a spherical Earth. (b) Ground range mapping for the same slant ranges r assuming a 1-hop propagation mode (i.e., ground backscatter) and an equivalent virtual reflection height at 300 km (blue dashed line). (c) Error in ground location obtained when applying the $\frac{1}{2}$-hop propagation assumption to 1-hop observations for three representative azimuthal beam directions; the black curve (ϕ_0=0°) corresponds to the radar boresight direction, while the purple and orange curves correspond to the beams furthest from boresight for a nominal 16- or 24-beam SuperDARN radar, respectively.

The differences in the ground ranges obtained assuming $\frac{1}{2}$-hop IS (Figure 2a) versus 1-hop GS (Figure 2b) at the same measured ranges and virtual height along the radar boresight direction ($\phi_0 = 0°$) can be seen in Figure 2c as indicated by the black curve. Here we find that using a $\frac{1}{2}$-hop IS propagation model can result in positive ground range offsets (i.e. away from the radar) of ∼60–150 km. Along the beam directions furthest from boresight for 16-beam ($\phi_0 = 25°$) or 24-beam ($\phi_0 = 38°$) SuperDARN radars, the difference in ground range increases to ∼150–200 km for higher elevation angles as indicated by the purple and orange curves, respectively. Compared to the standard SuperDARN range resolution of 45 km, this ground range error is quite significant and must be accounted for when comparing radar measurements to land or sea features.

In this study, we examine how HF propagation characteristics of IS observed at mid-latitudes compare to the previously derived VHMs for high-latitude propagation conditions. We also present the first statistical characterization of virtual height for different GS propagation modes. We use these results to derive a new VHM which can more accurately describe the propagation characteristics of both IS and GS measurements observed by the mid-latitude SuperDARN radars, thus allowing for improved geolocation of these LOS observations not only in ground range but also in azimuth.

2 Methodology and Data

In this study we use 5 years of data (2014–2018) from the mid-latitude Christmas Valley East (CVE) and Christmas Valley West (CVW) pair of co-located SuperDARN radars (43.27° N, 120.36° W). Figure 3 shows the nominal fields of view (FOVs) of each radar in geographic coordinates using the standard VHM, with contours of constant MLAT in Altitude-Adjusted Corrected Geomagnetic Coordinates (AACGM) (Shepherd, 2014) overlaid in blue. Both the CVE and CVW radars scan through up to 24 azimuthal beam directions across a sector of the mid- to high-latitude ionosphere spanning from 50°–80° MLAT. Each radar beam is separated by 3.24° in azimuth and sampled in 45 km range gates out to a maximum range of ∼5000 km at a cadence of 1–2 min. In practice however, only the 20 most-meridional beams of the CVE and CVW radars are typically sampled in order to synchronize scans to a 1 min boundary for standard radar operating modes.

LOS velocities, power, and spectral width are obtained from the raw data samples using the FITACF 2.5 library contained in version 4.3.1 of the Radar Software Toolkit (RST) (Thomas et al., 2020). Elevation angles are calculated using the generalized algorithm of Shepherd (2017) with fixed $t_{\rm diff}$ values of -398 ns and -346 ns for the CVE and CVW radars, respectively (Chisham et al., 2021). More than 450 million fitted LOS measurements with reliable elevation angles are available from each of the two radars during this 5-year interval, of which approximately 20% are identified as ionospheric scatter (IS) and 80% as ground scatter (GS) echoes using the default SuperDARN GS criterion:

$$|v| + \frac{w}{3} < 30 \text{ m/s} \tag{8}$$

where v is the fitted Doppler velocity and w is the spectral width. Note that echoes from meteor trails at near-ranges or slow-moving IS may be mis-identified as GS using the simple empirical criterion of Equation 8, particularly at mid-latitudes (Ribeiro et al., 2011). We will address the impact of potentially mis-identified scatter on our results in the following sections.

Figure 4 presents histograms of IS and GS echo occurrence for the CVE radar organized by six parameters: slant range, elevation angle, azimuthal beam number, radar operating frequency, Universal Time (UT), and month of year (all results for the CVW radar are shown in an equivalent set of figures in the supplementary material, and are generally similar to those shown for CVE). There is a large population of both IS and GS echoes found for slant ranges < 600 km which is likely associated with $\frac{1}{2}$-hop backscatter from either meteor trails or E-region irregularities (Makarevich, 2010; Yakymenko et al., 2015). Secondary peaks in the IS and GS distributions in Figure 4a are located at slant ranges of ∼1200 and ∼1500 km, respectively. Both scatter types are observed across the full range of measurable elevation angles from 0° to 50° with a clear peak at 18° elevation (Figure 4b). The discontinuities seen above 35° elevation are related to the maximum observable elevation angle by the CVE radar, which for a given radar's antenna configuration varies with both azimuthal beam direction and operating frequency

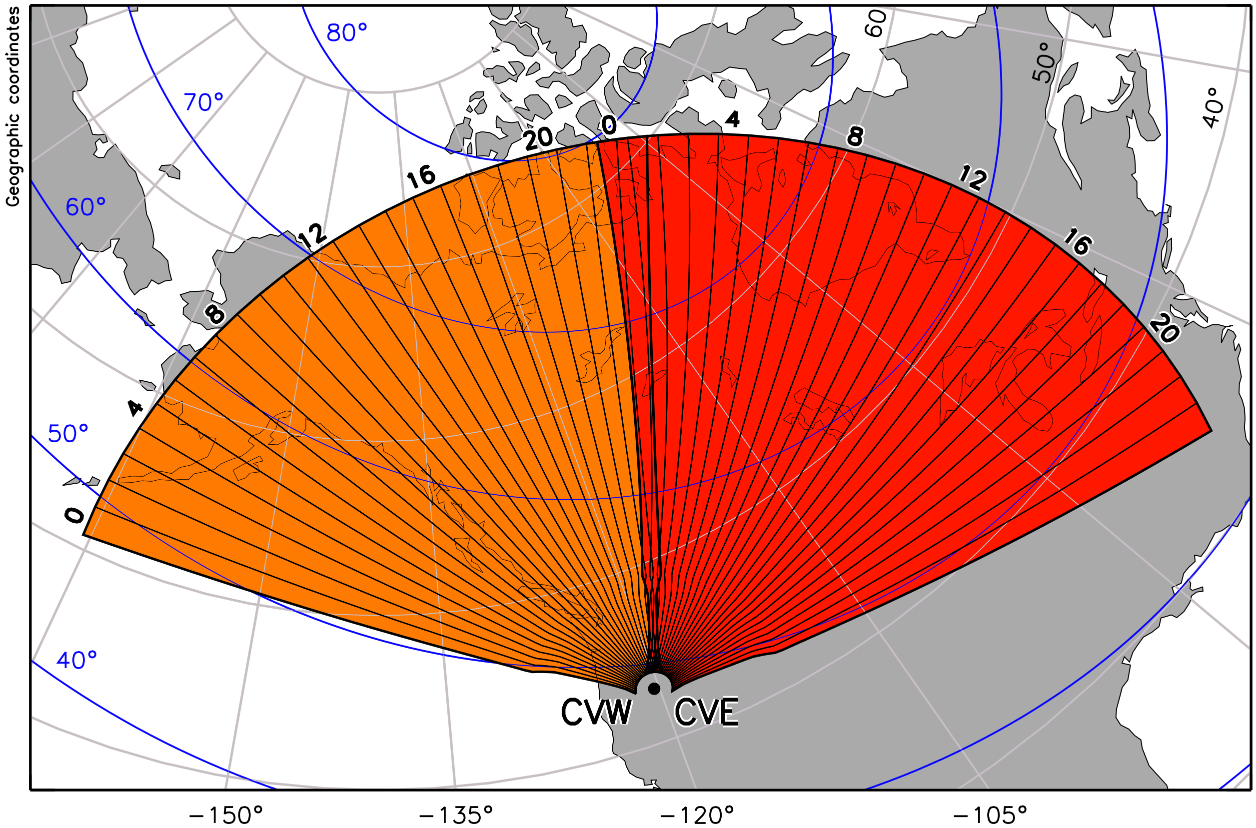

Figure 3. Nominal fields of view of the Christmas Valley East (CVE) and Christmas Valley West (CVW) radars in geographic coordinates, shaded red and orange respectively. Selected azimuthal beam numbers are labeled for each radar and contours of constant geomagnetic latitude at 10° intervals are overlaid in blue.

(Shepherd, 2017; Chisham, 2018). As previously described, the Christmas Valley radars typically operate on only the 20 most-meridional beams; for the CVE radar this corresponds to beam numbers 0–19 (Figure 4c). Beam number 10 of the CVE radar is the designated "camping" beam used for special operating modes where finer temporal resolution (and thus increased occurrence rate) is obtained along a single azimuthal direction, at the expense of an increased scan duration across the full radar FOV.

Figure 4d shows that the CVE radar typically operates in one of two frequency bands: 10.3–10.8 MHz (during nighttime) and 14.7–15.0 MHz (during daytime). The lower frequency band (10.3–10.8 MHz) has the appearance of being further divided into two bands separated by only a few hundred kHz, which is due to an unresolved software issue in the Christmas Valley radars' clear frequency search algorithm. By combining the echo occurrence from each of these lower (nighttime) frequency bands, approximately twice as many IS echoes are observed than at the higher (daytime) frequency band. The opposite is true for the GS data, with significantly more echoes observed at the higher (daytime) frequency band than for the lower (nighttime) band(s). Returning to the elevation histograms in Figure 4b, the maximum observable elevation angle at the lower frequency band ranges from ∼50° (at boresight) to ∼41° (furthest from boresight), while the elevation cutoff ranges from ∼41°–35° for the higher frequency band.

There is a clear diurnal variation in the GS occurrence seen in Figure 4e, with more GS echoes observed during daytime hours (14–02 UT) than at nighttime. We find the

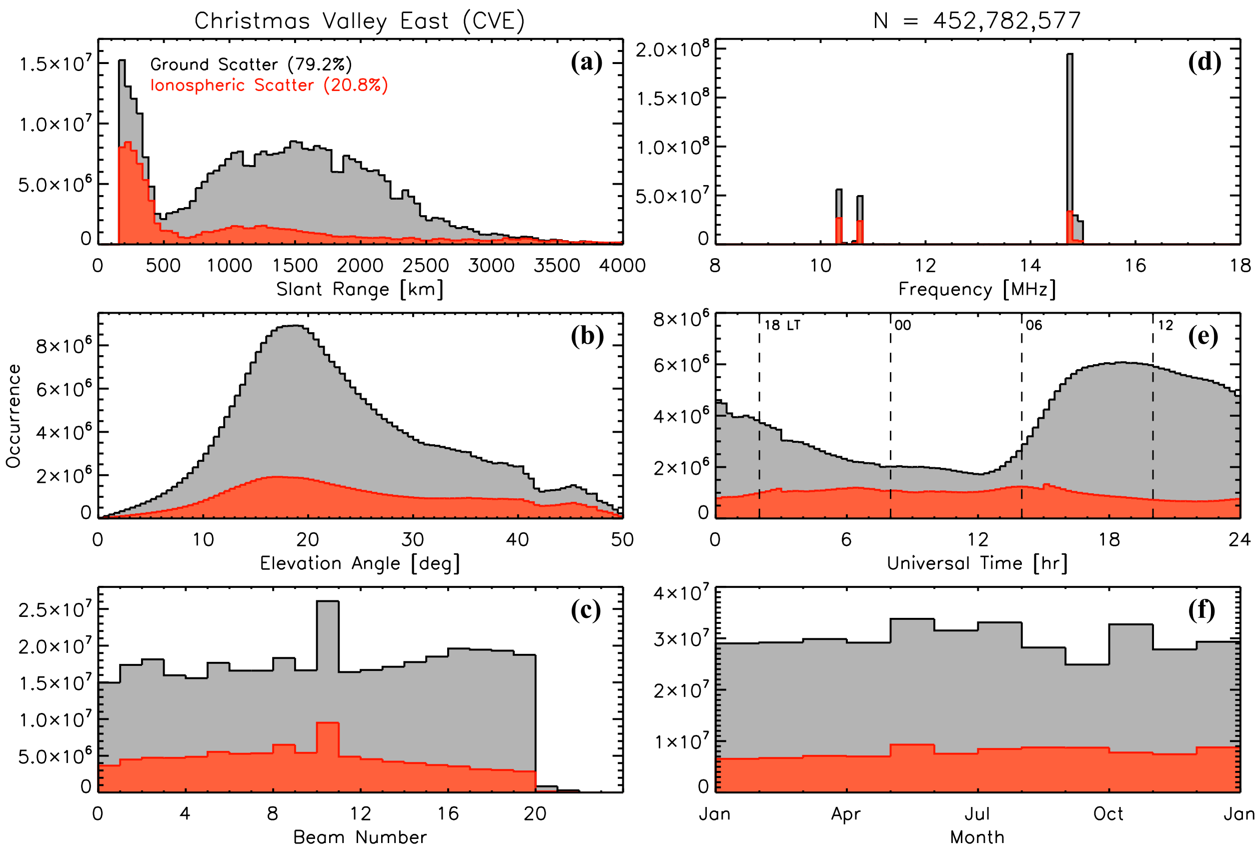

Figure 4. Statistical occurrence of CVE radar observations from 2014–2018 with (a) slant range, (b) elevation angle, (c) azimuthal beam number, (d) frequency, (e) Universal Time, and (f) month, sorted by ionospheric scatter (red) and ground scatter (black). Approximate local times at 6 hr intervals are indicated on panel (e) by vertical dashed lines, and the total number of measurements is given above panel (d).

opposite to be true for IS occurrence with slightly greater occurrence during nighttime (02–14 UT) than daytime hours. No clear seasonal variations in the IS occurrence are observed in Figure 4f and only a slight peak in the GS occurrence may be present during summer months (May–July). These results are largely in agreement with previous studies of SuperDARN backscatter occurrence rates at both mid- and high-latitudes (e.g., Hosokawa & Nishitani, 2010; Ribeiro et al., 2012; Ruohoniemi & Greenwald, 1997; Ballatore et al., 2000; Koustov et al., 2004; Ghezelbash et al., 2014; Koustov et al., 2019; Marcucci et al., 2021).

3 Results

3.1 Ionospheric and Ground Backscatter Distributions

We begin by considering the distribution of ionospheric and ground scatter observed by the CVE radar in terms of the measured elevation angle versus slant range. The top row of Figure 5 shows the joint probability distributions for both IS and GS, while the bottom row shows the same distributions normalized by the maximum occurrence at each range bin, after Chisham et al. (2008) and Chisham et al. (2021). The distributions in

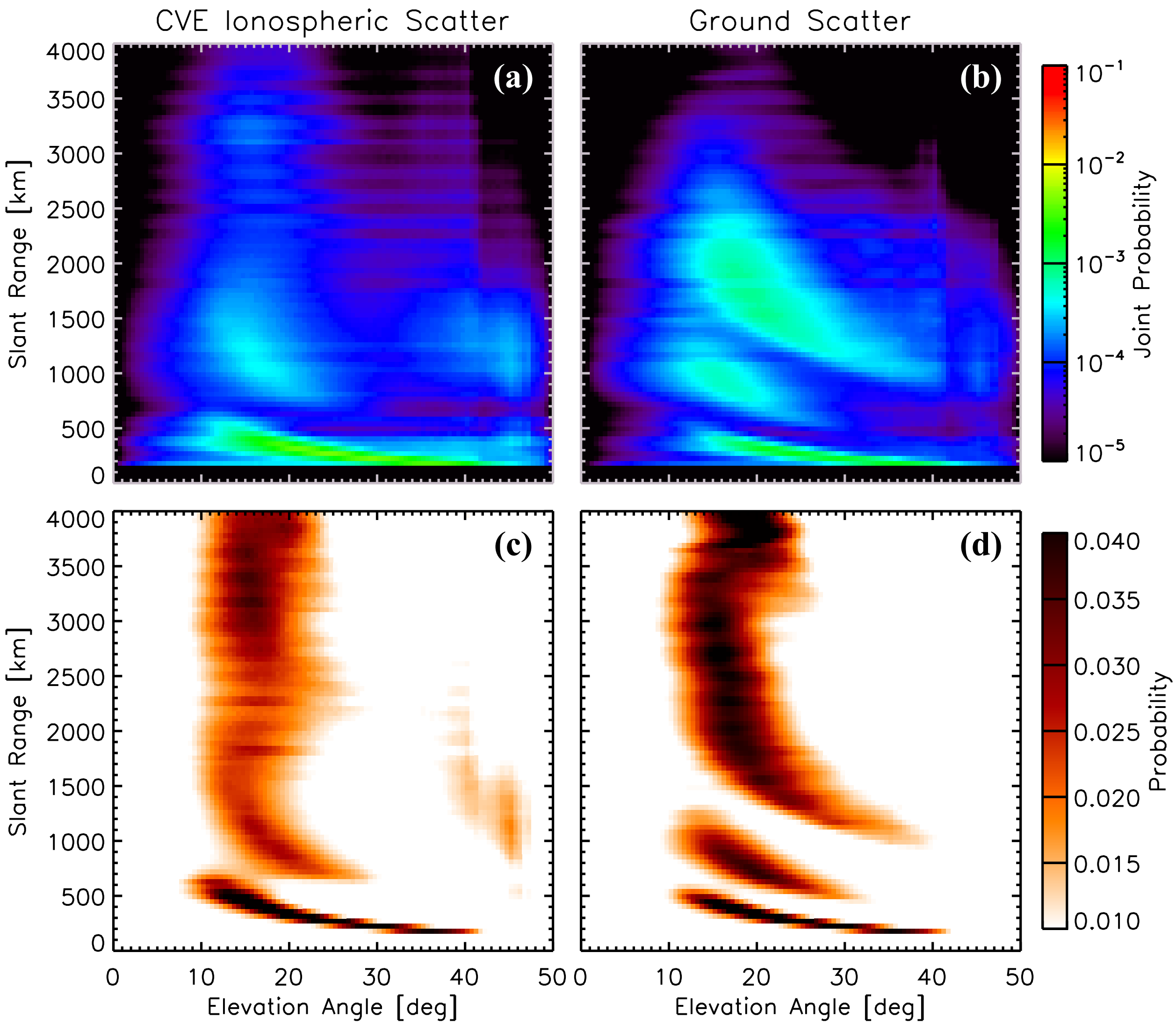

Figure 5. (top) Joint probability distributions of elevation angle and slant range observed by the CVE radar for (a) ionospheric and (b) ground scatter, in 0.5° elevation and 45 km range bins. (bottom) The same probability distributions normalized by the maximum occurrence in each range bin, after Chisham et al. (2008) and Chisham et al. (2021); occurrence probabilities of less than 0.010 are not shown.

each panel of Figure 5 are divided into 0.5° elevation and 45 km range bins. Starting with the IS distribution in Figures 5a and 5c, we observe three distinct populations:

1. At near ranges (∼180–600 km) across all elevation angles
2. Between ∼600–2000 km range and 10–30° elevation
3. At far ranges beyond ∼2500 km from 10–25° elevation

There is one other population observed at higher elevation angles (35–50°) between 600–2500 km range (seen most clearly in Figure 5c). This region of range-elevation space is sometimes associated with observations from the rear FOV (e.g., Milan et al., 1997; André et al., 1998). However, we consider this scenario unlikely due to the Christmas

Valley radars' twin-terminated dipole (TTFD) wire antenna and corner reflector design which has an improved front-to-back ratio compared to the log-periodic antenna design of the original SuperDARN radars (Custovic et al., 2013). Instead, these anomalous measurements are almost certainly aliased from low elevation angles near zero degrees (McDonald et al., 2013) and are therefore excluded from further analysis.

Next we consider the GS distribution shown in Figures 5b and 5d, and again observe three distinct populations:

1. At near ranges (∼180–500 km) across all elevation angles
2. Between ∼500–1500 km range and 10–30° elevation
3. Between ∼800–3000 km range and 10–40° elevation

Unlike the IS distribution shown in the left column of Figure 5, there is considerable overlap between each of these three GS populations in the range dimension along the vertical axis. Elevation angle information is therefore critical for the identification of different GS propagation modes. From the normalized elevation-range distribution shown in Figure 5d, there appears to be a discontinuity near 3500 km slant range where the center of the elevation distribution shifts from ∼14° to ∼19°. This feature may indicate the presence of multi-hop GS echoes observed at extreme ranges. Note the two populations of what we assume to be aliased elevation angles near 40° and 45° are visible in Figure 5b but not the normalized representation in Figure 5d; these aliased data are also excluded from further analysis.

3.2 Comparison to Existing Virtual Height Models

To aid in our physical interpretation of the results presented in Figure 5, we can use the measured elevation angle and slant range information to calculate the virtual height of the IS and GS probability distributions for any arbitrary number of hops with Equation 1. By doing so we may also evaluate the performance of existing SuperDARN VHMs when applied to the mid-latitude Christmas Valley radar observations. The resulting virtual height profiles, when assuming a $\frac{1}{2}$-hop propagation mode (e.g., Figure 1a), are shown versus range in Figures 6a and 6b for the normalized IS and GS probability distributions, respectively. The standard VHM with an F-region virtual height h_i of 300 km is overlaid on each panel in blue for reference (Equation 4). At near ranges in Figure 6a, there is excellent agreement between the observations and model prediction of 115 km virtual height, suggesting these echoes are in fact associated with $\frac{1}{2}$-hop backscatter from either meteor trails or E-region irregularities. Beyond ∼600 km range the IS distribution shifts from E- to F-region altitudes, and quickly curves upwards and away from the standard VHM h_i which remains constant at 300 km virtual height.

After careful examination of the elevation-range and range-height distributions, we estimate the transition between $\frac{1}{2}$- and $1\frac{1}{2}$–hop F-region IS propagation modes to be located near 2270 km slant range for the Christmas Valley radars. Figure 6c shows the same IS distribution as panel (a) but instead applying a $1\frac{1}{2}$–hop propagation assumption to the observations beyond 2270 km range (e.g., Figure 1c). This approach has the practical effect of lowering the virtual height by ∼700–1400 km in our assumed $1\frac{1}{2}$–hop region. Figure 6e shows the difference in ground range obtained when using the $\frac{1}{2}$- and $1\frac{1}{2}$-hop assumptions applied in Figure 6c versus the predictions from the standard VHM. Here, a positive ground range difference indicates the standard VHM places the scatter farther from the radar than Equations 1 and 2 would suggest. The ground range of the E-region IS is largely consistent whether the model or measured elevation angles are used, while the $\frac{1}{2}$–hop F-region IS can be located 0–400 km closer to the radar than the standard VHM predicts. The $1\frac{1}{2}$–hop F-region IS is seen to always be in error with ground range differences of 100–600 km found for all ranges, again with the model placing scatter further from the radar than the measurements suggest.

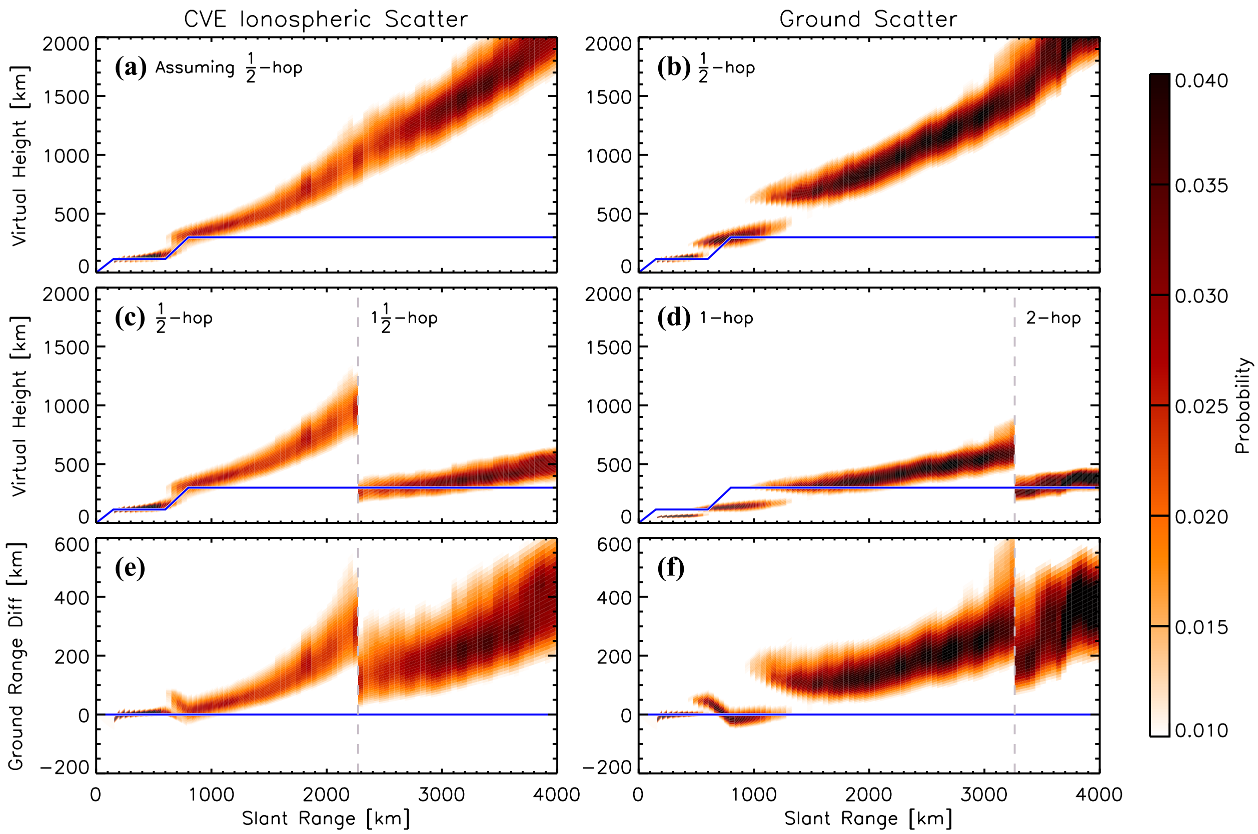

Figure 6. Normalized probability distribution of elevation angle and slant range observed by the CVE radar for (a) ionospheric and (b) ground scatter from Figure 5 mapped to slant range versus virtual height assuming a $\frac{1}{2}$-hop propagation path, with the standard VHM overlaid in blue. (c) Same probability distribution for ionospheric scatter as panel (a) but assuming a $1\frac{1}{2}$-hop propagation mode for slant ranges beyond 2250 km (vertical dashed line). (d) Same probability distribution for ground scatter as panel (b) but assuming a 1-hop propagation mode for slant ranges less than 3240 km (vertical dashed line) and a 2-hop propagation mode for further ranges. The bottom row shows the difference in ground ranges for (e) ionospheric and (f) ground scatter from panels (c) and (d) compared to application of the standard VHM (which always assumes a $\frac{1}{2}$-hop propagation path); positive values indicate the true ground range is closer to the radar than suggested by the model.

The GS distribution shown in Figure 6b has similarly been mapped to virtual height assuming a $\frac{1}{2}$-hop propagation mode using Equation 1. We see that again at near ranges (180–500 km) the observations and standard VHM agree quite closely. This agreement suggests the data have been mis-identified as GS and are instead associated with $\frac{1}{2}$-hop backscatter from either meteor echoes or E-region irregularities, as the virtual height at these ranges is unphysically low ($\sim$50 km) when assuming a 1-hop propagation mode (Figure 6d). The GS distribution at intermediate ranges (500–1300 km) in Figure 6b is located between 250–400 km virtual height, straddling the standard VHM F-region h_i of 300 km. However, the virtual height of this population, when calculated assuming a 1-hop propagation mode, also agrees with the standard VHM E-region virtual height of 115 km (Figure 6d), suggesting the echoes may be attributed to either mis-identified $\frac{1}{2}$-hop IS from F-region irregularities or 1-hop GS reflected at E-region altitudes.

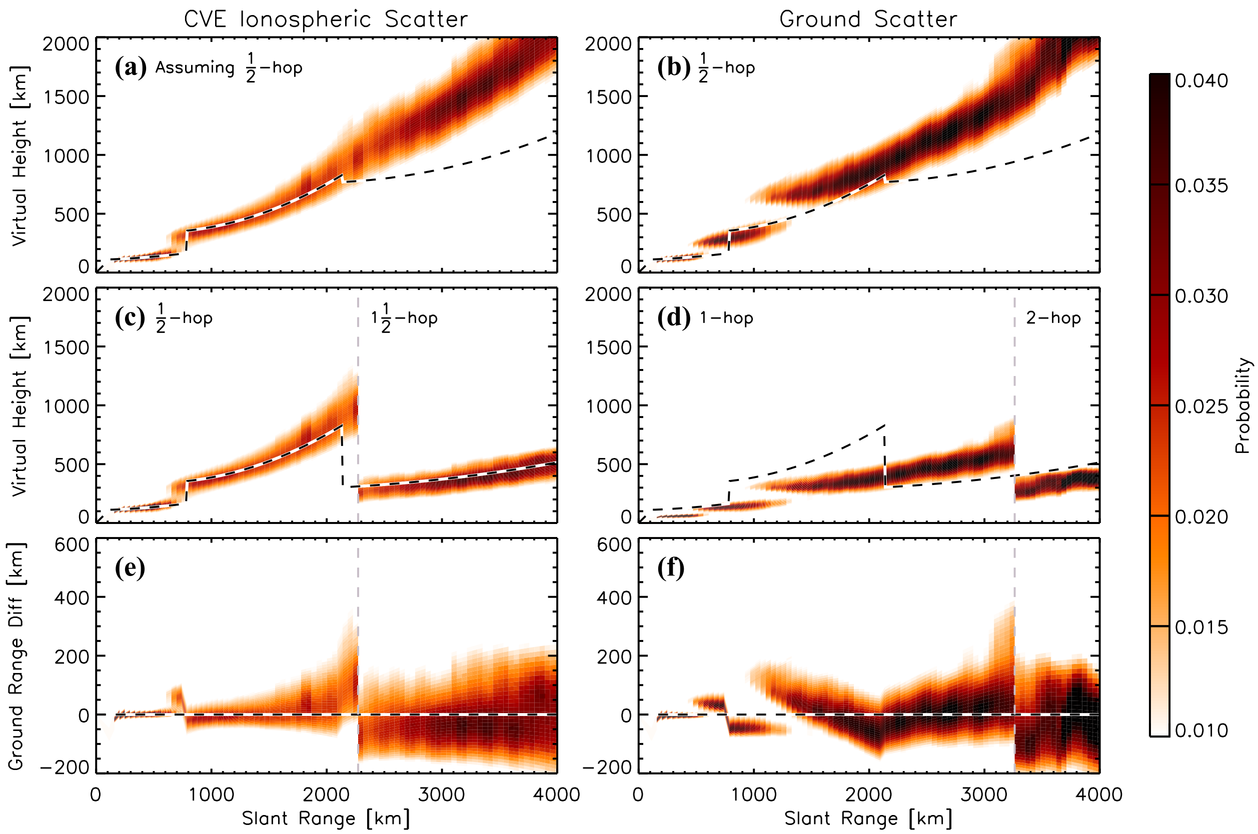

Figure 7. Normalized probability distributions of slant range and virtual height observed by the CVE radar for (left) ionospheric and (right) ground scatter in the same format as Figure 6, but instead compared against the Chisham VHM overlaid as a black and white dashed line. The "pseudo" virtual height predicted by the Chisham VHM for $1\frac{1}{2}$-hop scatter (beyond 2137 km slant range) is overlaid on panels (a–b), while the "true" virtual height predicted by the model for $1\frac{1}{2}$-hop scatter is overlaid on panels (c–d); see text for further details. The bottom row shows the difference in ground ranges for (e) ionospheric and (f) ground scatter from panels (c) and (d) compared to application of the Chisham VHM (which assumes either a $\frac{1}{2}$-hop or $1\frac{1}{2}$-hop propagation path); positive values indicate the true ground range is closer to the radar than suggested by the model.

At farther ranges (beyond ∼1000 km), the GS distribution in Figure 6b is offset from the standard VHM prediction by at least 300 km and curves upwards to virtual heights exceeding 2000 km. After applying a 1-hop propagation assumption to these data (e.g., Figure 1b) the distribution is brought downward to significantly lower virtual heights spanning from 300–800 km. Again we have estimated a likely transition between 1- and 2-hop F-region GS to be located near 3260 km slant range, beyond which the observations in Figure 6d have been mapped to a virtual height assuming a 2-hop propagation mode using Equation 1. Similar to Figure 6e, Figure 6f shows the difference in ground range obtained when using the 1- and 2-hop assumptions applied in Figure 6d versus the predictions from the standard VHM.

Figure 7 is in the same format as Figure 6, but instead we compare the CVE results to the Chisham VHM (black and white dashed line) rather than to the standard VHM. In the top row, the IS and GS distributions are again mapped to range-virtual height space assuming a $\frac{1}{2}$-hop propagation mode. In these panels, the "pseudo" virtual height of the Chisham VHM is shown for the $1\frac{1}{2}$-hop region beyond 2137 km range. Chisham et al. (2008) derived this pseudo virtual height for compatibility with the existing SuperDARN range finding software, which can support only $\frac{1}{2}$-hop propagation modes. The pseudo virtual height is therefore a $\frac{1}{2}$-hop virtual height with the same ground range as the true $1\frac{1}{2}$-hop virtual height found by Chisham et al. (2008) in their statistical analysis of IS echoes. In the middle row of Figure 7 where the observed IS and GS distributions have been mapped using more appropriate assumptions, the true $1\frac{1}{2}$-hop virtual height predicted by the Chisham VHM is shown. Here we see that the IS distribution aligns quite well with the Chisham VHM in all three scatter regions in terms of virtual height, except perhaps the $1\frac{1}{2}$-hop region where the observations are located slightly below the model prediction. Where the IS observations and Chisham VHM differ most noticeably are the ranges at which the peak of the virtual height distribution transitions from one propagation mode to the next, i.e. $\frac{1}{2}$-hop E-region to $\frac{1}{2}$-hop F-region, and $\frac{1}{2}$- to $1\frac{1}{2}$-hop F-region. This difference is further illustrated in Figure 7e, where the ground range differences are largely centered about zero except at these propagation boundaries.

The GS distribution shown on the right side of Figure 7, on the other hand, does not align particularly well with the Chisham VHM. The $\frac{1}{2}$-hop F-region portion of the Chisham VHM is at significantly higher virtual heights than the 1-hop F-region height, and the 2-hop GS is at a lower virtual height than the $1\frac{1}{2}$-hop model prediction. However, an incorrect virtual height and propagation mode can sometimes produce a realistic ground range estimate. For example, at 3500 km slant range the Chisham VHM predicts a $1\frac{1}{2}$-hop propagation mode with a virtual height of 435 km and ground range of 3146 km, while for a 2-hop propagation mode at that range the CVE GS measurements suggest a virtual height of 315 km and ground range of 3189 km (only a $\sim$1% difference of 43 km, or less than one standard range gate). At these ranges the elevation angle difference is less than 1° so the azimuthal errors will be within the beamwidth (3.24°), however at nearer ranges when the ground ranges agree but the virtual height is incorrect, the errors in elevation angle, and therefore azimuth, will become more significant.

3.3 Christmas Valley Virtual Height Model

Figure 8 shows results for both the CVE and CVW radars in range-virtual height space, with the IS and GS distributions again in the left and right columns, respectively. The green lines overlaid on panels (a–d) indicate the virtual height of peak occurrence at each slant range bin, i.e. the virtual height at which observations are most likely for each range bin. Note there is significant overlap in range between the 1-hop E- and 1-hop F-region GS distributions observed by both radars (Figures 8b and 8d), even moreso for CVW. In this case we have attempted to find the peak occurrence for each virtual height population regardless of whether there is some overlap in range.

The virtual height of maximum occurrence at each range bin is shown for both radars in Figures 8e and 8f with results for CVE in black and CVW in blue. In the same manner as Chisham et al. (2008), we have performed a least-squares fit to the average of the black and blue curves using a quadratic function (Equation 5), which is overlaid on Figures 8e and 8f in red. The red curves therefore correspond to the Christmas Valley virtual height model derived from both CVE and CVW observations, referred to hereafter as the CV VHM, with 3 independent sets of coefficients for both the IS and GS propagation modes. These model coefficients for Equation 5 are provided in Table 2. Note that although we have shown an abrupt transition from $\frac{1}{2}$- to $1\frac{1}{2}$-hop F-region propagation modes indicated by the vertical dashed line, this should in practice be a flexible boundary where the transition may vary based on local time, season, or solar cycle conditions (and similarly for the $\frac{1}{2}$-hop E- to F-region transition).

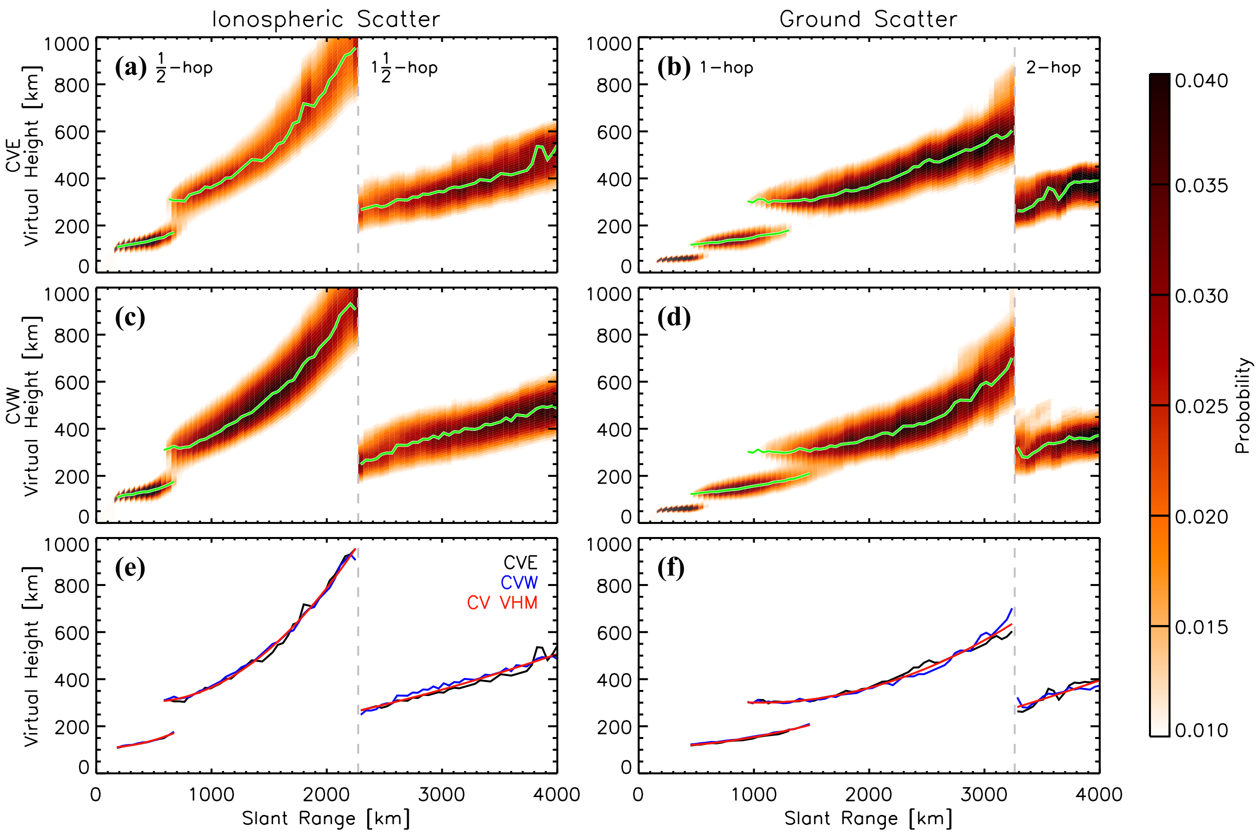

Figure 8. Normalized probability distributions of slant range and virtual height observed by the CVE (top row) and CVW (middle row) radars for ionospheric scatter (left column) and ground scatter (right column), with the virtual height of maximum occurrence at each range bin overlaid on panels (a–d) in green. The bottom row shows the virtual height of maximum occurrence from the CVE and CVW radars in black and blue, respectively, with a series of quadratic fits representing the new VHM overlaid in red. Note the different vertical axis scale used in these panels compared to Figures 6 and 7.

To assess the performance of the CV VHM relative to the standard and Chisham VHMs, we calculate the ground range difference of all IS and GS observations when using each of the three VH models. These results are summarized in Figure 9, where each panel corresponds to a separate IS or GS propagation mode; results for the standard VHM are shown in gray, the Chisham VHM in blue, and the CV VHM in red. We can see that for all six propagation modes, the ground range difference when using the CV VHM is centered about zero, indicating there are no systematic biases (as is clearly seen for the standard VHM with positive range offsets). The Chisham VHM performs surprisingly well even for the 1- and 2-hop F-region GS propagation modes, although it is worth noting that because the Chisham VHM virtual heights are incorrect, the inferred elevation angle and thus coning angle correction to the beam azimuth will be incorrect (Equation 7).

4 Discussion

The IS component of the CV model has large deviations from the SuperDARN community's standard VHM which uses fixed E- and F-region virtual heights of 115 and 300 km respectively (Equation 4). The IS component of the CV model agrees much more closely

Table 2. The coefficients for Equation 5 for the Christmas Valley ionospheric and ground scatter VHM.

Model	Propagation Mode	A	B	C
Ionospheric Scatter	$\frac{1}{2}$-hop E-region	108.873	-0.01444	1.57806×10^{-4}
	$\frac{1}{2}$-hop F-region	341.005	-0.17484	1.99144×10^{-4}
	$1\frac{1}{2}$-hop F-region	92.9665	0.03967	1.59501×10^{-5}
Ground Scatter	1-hop E-region	111.393	-1.65773×10^{-4}	4.26675×10^{-5}
	1-hop F-region	378.022	-0.14738	6.99712×10^{-5}
	2-hop F-region	-76.2406	0.06854	1.23078×10^{-5}

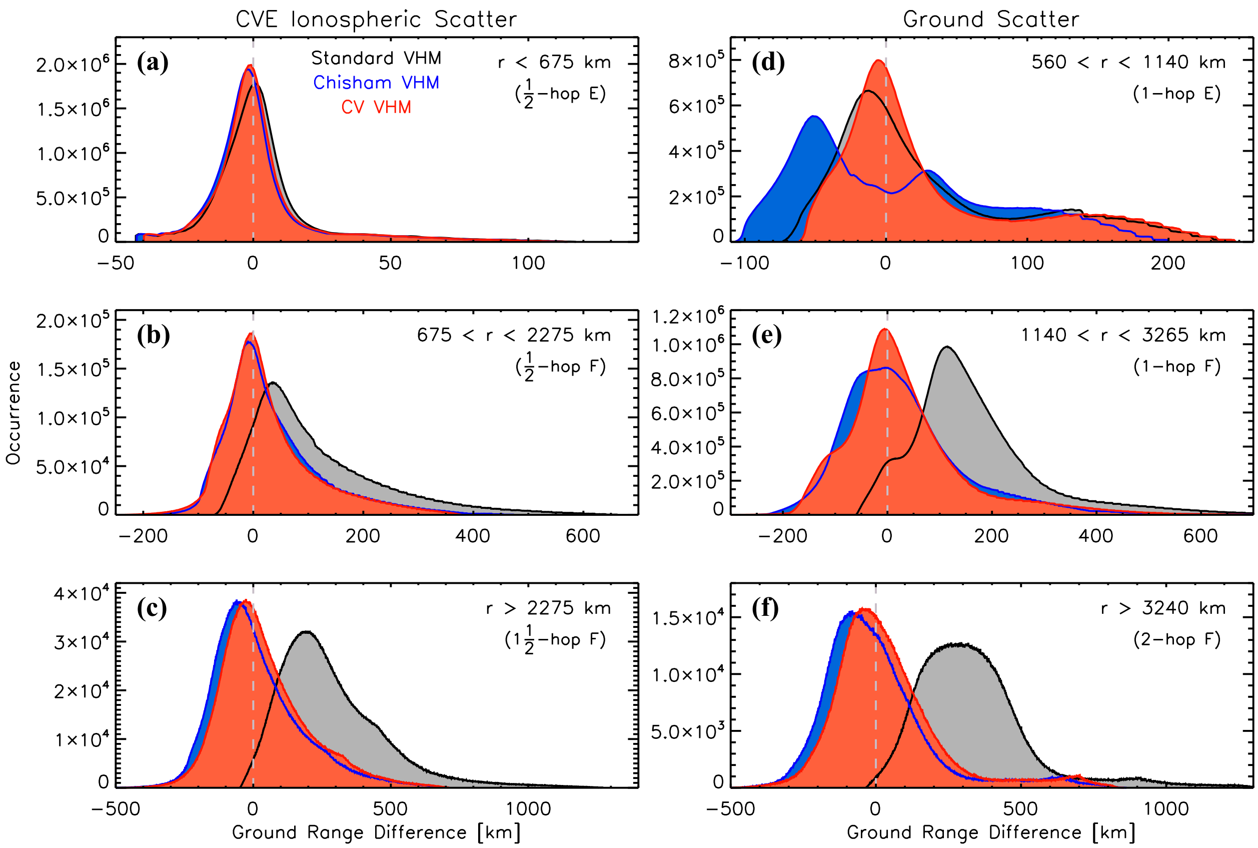

Figure 9. Differences in ground range when using the slant range and virtual height observed by the CVE radar for (left) ionospheric and (right) ground scatter compared to the standard (gray), Chisham (blue) and CV (red) virtual height models. Results are organized by (a) $\frac{1}{2}$-hop E-region, (b) $\frac{1}{2}$-hop F-region, (c) $1\frac{1}{2}$-hop F-region, (d) 1-hop E-region, (e) 1-hop F-region, and (f) 2-hop F-region scatter distributions.

with the Chisham VHM, suggesting that, in a statistical sense, the $\frac{1}{2}$- and $1\frac{1}{2}$-hop propagation modes are consistent between mid- and high-latitude radar observations (or at least for the CVE/CVW and SAS radars, from which the respective models were derived). Where the CV and Chisham VHM differ the most are the ranges at which the models predict a transition from $\frac{1}{2}$-hop E- to $\frac{1}{2}$-hop F-region modes, and from $\frac{1}{2}$-hop to $1\frac{1}{2}$-hop F-region modes. While a fixed transition range is necessary for implementation in automated geolocation software, ideally these should be flexible boundaries which the user can shift to nearer or further ranges depending on instantaneous conditions. These transition ranges (as well as the virtual height) are also likely to vary with local time, season, operating frequency, etc., and will be examined in future work. We also emphasize that despite the Chisham VHM providing reasonably accurate ground ranges when applied to 1- or 2-hop F-region GS propagation modes (Figure 9e–f), the resulting elevation angles and thus coning angle correction to the radar beam azimuth will be incorrect. This additional error in ground location due to an incorrect elevation angle predicted by any VHM is an often overlooked aspect of SuperDARN HF backscatter geolocation.

The greatest source of uncertainty when applying the CV VHM described in this study will likely arise from the initial determination of whether a backscatter echo belongs to either an IS or GS propagation mode. This issue was not relevant for previous VHMs, as they did not consider GS propagation modes. Ribeiro et al. (2011) and others have demonstrated how the default SuperDARN GS criteria can falsely identify slow-moving IS as GS, particularly at subauroral latitudes in the nightside ionosphere. Existing techniques for identifying SuperDARN backscatter propagation modes (e.g., Burrell et al., 2015; Bland et al., 2014) rely upon calibrated elevation angle measurements, which are currently not available at many SuperDARN radar sites.

In our study, we have identified a backscatter region of ambiguous origin located between ∼500–1400 km slant range where the data could belong to either a $\frac{1}{2}$-hop F-region or 1-hop E-region propagation mode. Figure 10 shows the CVE echo distribution in range-virtual height space centered about this region for IS-flagged data in panel (a) and GS-flagged data in panel (b); both distributions are mapped to virtual height assuming a $\frac{1}{2}$-hop propagation mode for easier comparison. The precise region of interest is indicated by the blue rectangle: approximately 12 million IS-flagged echoes and 58 million GS-flagged echoes are located within this space (a similar proportion to the overall IS-GS echo ratio, e.g. Figure 4a). In the lower panels of Figure 10 we have plotted data from the echo region of "ambiguous" origin in terms of the joint UT versus month/year probability distribution. The black and white dashed lines overlaid on each panel indicate the local sunrise and sunset times at the approximate midpoint between the CVE radar boresight direction and backscattering volume. The outer histograms along the top and right edges of each panel show the 1-D occurrence distributions with UT and month/year, respectively. Overlaid on the right-hand histogram in red is the monthly average F10.7 solar radio flux (Tapping, 2013). We again refer the reader to the online supplementary material for an equivalent figure of the region of "ambiguous" scatter origin observed by the CVW radar.

Starting with the IS-flagged echo occurrence in Figure 10c, there is a clear dependence on the solar terminator with increased occurrence in the hours just after local sunset (∼0–8 UT depending on season). This dependence is superimposed on a larger trend of increasing echo occurrence with decreasing F10.7 (i.e., the decline of solar cycle 24). Ribeiro et al. (2012) found a similar relationship between the solar terminator and nighttime IS echo occurrence as observed by the mid-latitude Blackstone radar (37.10° N, 77.95° W), although they could not identify any seasonal or solar cycle trends because their study was limited to only 2 years of data. There is an abrupt increase in the total occurrence near the end of 2015, which we are unable to attribute to any operational changes at the CVE radar (CVW did not observe a similar change in scatter occurrence). Throughout all years in this interval, there is also a smaller population of daytime echoes observed only during summer months. We therefore suggest that the IS-flagged distribution contains primarily backscatter from nighttime ionospheric sources with some contamination from daytime 1-hop E-region propagation modes.

Turning next to the GS-flagged echoes in Figure 10d, there is a much more even distribution of daytime and nighttime echoes seen in the UT histogram along the top of the figure. Again there are signs of increased echo occurrence following the local sun-

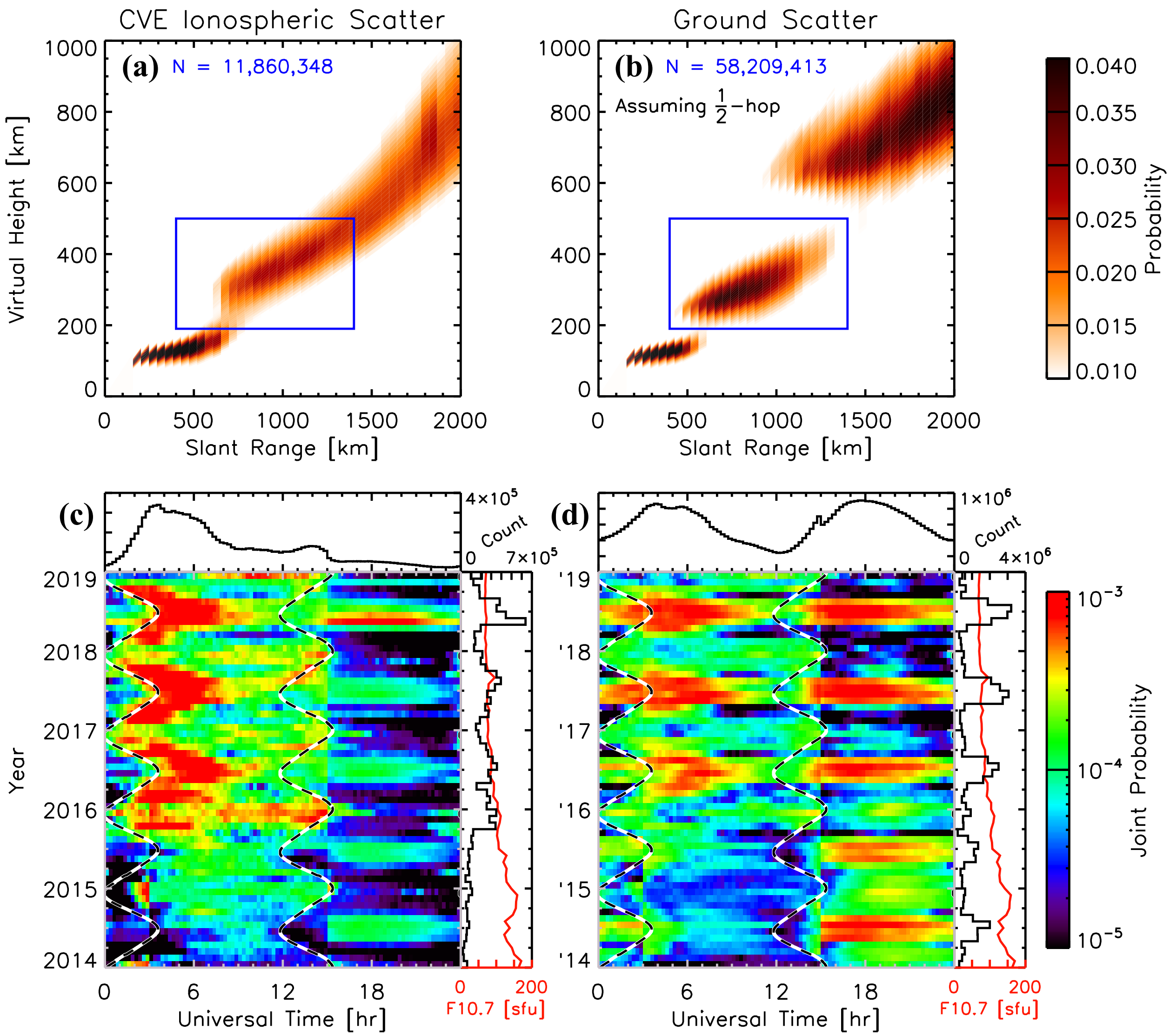

Figure 10. Normalized probability distributions of slant range and virtual height observed by the CVE radar for (a) ionospheric scatter and (b) ground scatter, centered on the region of possible "mixed" scatter indicated by the blue box. Both the ionospheric and ground scatter-flagged data in panels (a–b) have been mapped to virtual height assuming a $\frac{1}{2}$-hop propagation mode for easier comparison, and the number of observations falling within the "mixed" scatter region are given at the top of each panel in blue. (c) Joint probability distribution of Universal Time (UT) and month/year for the ionospheric-flagged scatter within the blue box in panel (a); along the top of the panel is a 1-D histogram of the same data as a function of UT only, while along the right side of the panel is a 1-D histogram as a function of month and year with the monthly average F10.7 solar radio flux overlaid in red. (d) Same as panel (c) but for the ground scatter-flagged data within the blue box in panel (b). Approximate sunrise and sunset times at the midpoint between the CVE radar and "mixed" scatter backscattering volume are overlaid on panels (c–d) as black and white dashed lines.

set terminator. The daytime summer population is present during all years, however, and appears to be a dominant contributor to the 1-D histogram along the right edge of the plot. This feature follows from the knowledge that mid-latitude E-region densities are almost solely controlled by solar zenith angle, i.e. maximum during summer and minimum during winter (Chu et al., 2009), and thus more likely to support a 1-hop E-region propagation mode. An increase in 1-hop E-region GS echo occurrence at mid-latitudes during summer months was also predicted by the ray-tracing simulations for the Blackstone radar by de Larquier et al. (2011) in their Figures 6 and 7. Unlike the IS-flagged results in our Figure 10c, in the GS-flagged results there is another weaker population of winter daytime echoes which disappears with decreasing F10.7 / declining solar cycle phase. This feature also follows from the knowledge that N_mE has a secondary dependence on F10.7 (Titheridge, 2000).

To summarize our observations of this measurement region, there is clear evidence for contamination of GS echoes in the IS-flagged data and vice versa. However, there is nearly an equal number of likely IS echoes in the GS-flagged data as there are true GS echoes. Therefore, even the inclusion of measured elevation angles in an empirical GS criteria will not be sufficient to accurately classify the measurements within this slant range interval as either IS or GS for the Christmas Valley radars. Because the ionospheric E-region electron densities are almost solely controlled by the solar zenith angle at mid-latitudes (with a secondary dependence on solar activity), consideration of local time, season, and solar cycle factors may help with discrimination of IS versus GS sources. Future work will determine whether echoes are observed by the other mid-latitude SuperDARN radars which exhibit similar occurrence characteristics.

5 Conclusions

In this study we have examined 5 years of data from the mid-latitude Christmas Valley East and West SuperDARN radars to derive an empirical virtual height model with two sets of coefficients: one suitable for ionospheric scatter (IS) and, for the first time, another exclusively for ground scatter (GS) echoes. Both components of the CV model represent a significant advancement over the standard SuperDARN virtual height model, which treats all backscatter echoes as belonging to either a $\frac{1}{2}$-hop E- or F-region IS propagation mode. The IS component of our CV model performs similarly to the more recent model of Chisham et al. (2008), suggesting that in a climatological sense, the HF propagation modes for backscatter from ionospheric irregularities are similar at both auroral and mid-latitudes. We have also identified a measurement region ($500 < r < 1400$ km) where the LOS velocity, spectral width, slant range, and elevation angle are insufficient for separation of IS and GS echoes. Local time, season, and solar cycle factors should therefore be considered when analyzing scatter from this region. The CV IS and GS virtual height models have been incorporated into the freely available SuperDARN RST for use with the standard analysis routines, which will improve the geolocation accuracy for scatter observed by all mid-latitude SuperDARN radars.

Open Research

The raw SuperDARN data used in this study are available from the British Antarctic Survey (BAS) SuperDARN data mirror (https://www.bas.ac.uk/project/superdarn). The Radar Software Toolkit (RST) to read and process the SuperDARN data can be downloaded from Zenodo (Thomas et al., 2020). The monthly average solar radio flux data were obtained from Space Weather Canada at https://spaceweather.gc.ca/solarflux/sx-5-en.php.

Acknowledgments

This research was funded by the National Science Foundation under grants OPP-1836426 and AGS-1341925. The authors acknowledge the use of SuperDARN data. SuperDARN is a collection of radars funded by the national scientific funding agencies of Australia, Canada, China, France, Italy, Japan, Norway, South Africa, UK, and United States. The authors also acknowledge the use of solar radio flux data from Space Weather Canada.

References

André, D., Sofko, G. J., Baker, K., & MacDougall, J. (1998). SuperDARN interferometry: Meteor echoes and electron densities from groundscatter. *J. Geophys. Res.*, *103*(A4), 7003–7015. doi: 10.1029/97JA02923

Ballatore, P., Villain, J. P., Vilmer, N., & Pick, M. (2000). The influence of the interplanetary medium on SuperDARN radar scattering occurrence. *Ann. Geophys.*, *18*, 1576–1583. doi: 10.1007/s00585-001-1576-2

Bilitza, D., McKinnell, L.-A., Reinisch, B., & Fuller-Rowell, T. J. (2011). The international reference ionosphere today and in the future. *J. Geod.*, *85*, 909–920. doi: 10.1007/s00190-010-0427-x

Bland, E. C., McDonald, J., de Larquier, S., & Devlin, J. C. (2014). Determination of ionospheric parameters in real time using SuperDARN HF radars. *J. Geophys. Res. Space Physics*, *119*, 5830–5846. doi: 10.1002/2014JA020076

Breit, G., & Tuve, M. (1926). A test of the existence of the conducting layer. *Phys. Rev.*, *28*, 554–575.

Bristow, W. A., Greenwald, R. A., & Villain, J. P. (1996). On the seasonal dependence of medium-scale atmospheric gravity waves in the upper atmosphere at high latitudes. *J. Geophys. Res.*, *101*(A7), 15685–15699. doi: 10.1029/96JA01010

Burrell, A. G., Milan, S. E., Perry, G. W., Yeoman, T. K., & Lester, M. (2015). Automatically determining the origin direction and propagation mode of high-frequency radar backscatter. *Radio Sci.*, *50*, 1225–1245. doi: 10.1002/2015RS005808

Chakraborty, S., Ruohoniemi, J. M., Baker, J. B. H., & Nishitani, N. (2018). Characterization of short-wave fadeout seen in daytime SuperDARN ground scatter observations. *Radio Sci.*, *53*, 472–484. doi: 10.1002/2017RS006488

Chisham, G. (2018). Calibrating SuperDARN interferometers using meteor backscatter. *Radio Sci.*, *53*, 761–774. doi: 10.1029/2017RS006492

Chisham, G., Burrell, A. G., Marchaudon, A., Shepherd, S. G., Thomas, E. G., & Ponomarenko, P. (2021). Comparison of interferometer calibration techniques for improved SuperDARN elevation angles. *Polar Sci.*, *28*, 100638. doi: 10.1016/j.polar.2021.100638

Chisham, G., Lester, M., Milan, S. E., Freeman, M. P., Bristow, W. A., Grocott, A., … Walker, A. D. M. (2007). A decade of the Super Dual Auroral Radar Network (SuperDARN): Scientific achievements, new techniques and future directions. *Surv. Geophys.*, *28*(1), 33–109. doi: 10.1007/s10712-007-9017-8

Chisham, G., & Pinnock, M. (2002). Assessing the contamination of SuperDARN global convection maps by non-F-region backscatter. *Ann. Geophys.*, *20*, 13–28. doi: 10.5194/angeo-20-13-2002

Chisham, G., Yeoman, T. K., & Sofko, G. J. (2008). Mapping ionospheric backscatter measured by the SuperDARN HF radars – Part 1: A new empirical virtual height model. *Ann. Geophys.*, *26*, 823–841. doi: 10.5194/angeo-26-823-2008

Chu, Y.-H., Wu, K.-H., & Su, C.-L. (2009). A new aspect of ionospheric E region electron density morphology. *J. Geophys. Res.*, *114*, A12314. doi: 10.1029/2008JA014022

Custovic, E., McDonald, A. J., Whittington, J., Elton, D., Kane, T. A., & Devlin, J. C. (2013). New antenna layout for a SuperDARN HF radar. *Radio Sci.*, *48*, 722–728. doi: 10.1002/2013RS005156

de Larquier, S., Ponomarenko, P., Ribeiro, A. J., Ruohoniemi, J. M., Baker, J. B. H., Sterne, K. T., & Lester, M. (2013). On the spatial distribution of decameter-scale subauroral ionospheric irregularities observed by SuperDARN radars. *J. Geophys. Res. Space Physics*, *118*, 5244–5254. doi: 10.1002/jgra.50475

de Larquier, S., Ruohoniemi, J. M., Baker, J. B. H., Ravindran Varrier, N., & Lester, M. (2011). First observations of the midlatitude evening anomaly using Super Dual Auroral Radar Network (SuperDARN) radars. *J. Geophys. Res.*, *116*, A10321. doi: 10.1029/2011JA016787

Frissell, N. A., Baker, J. B. H., Ruohoniemi, J. M., Gerrard, A. J., Miller, E. S., West, M. L., & Bristow, W. A. (2016). Sources and characteristics of medium-scale traveling ionospheric disturbances observed by high-frequency radars in the North American sector. *J. Geophys. Res. Space Physics*, *121*, 3722–3739. doi: 10.1002/2015JA022168

Gauld, J. K., Yeoman, T. K., Davies, J. A., & Milan, S. E. (2002). SuperDARN radar HF propagation and absorption response to the substorm expansion phase. *Ann. Geophys.*, *20*, 1631–1645. doi: 10.5194/angeo-20-1631-2002

Ghezelbash, M., Fiori, R. A. D., & Koustov, A. V. (2014). Variations in the occurrence of SuperDARN F region echoes. *Ann. Geophys.*, *32*, 147–156. doi: 10.5194/angeo-32-147-2014

Greenwald, R. A., Baker, K. B., Dudeney, J. R., Pinnock, M., B., J. T., Thomas, E. C., ... Yamagishi, H. (1995). DARN/SuperDARN: A global view of the dynamics of high-latitude convection. *Space Sci. Rev.*, *71*(1), 761–796. doi: 10.1007/BF00751350

Greenwald, R. A., Baker, K. B., Hutchins, R. A., & Hanuise, C. (1985). An HF phased-array radar for studying small-scale structure in the high-latitude ionosphere. *Radio Sci.*, *20*(1), 63–79. doi: 10.1029/RS020i001p00063

Greenwald, R. A., Frissell, N., & de Larquier, S. (2017). The importance of elevation angle measurements in HF radar investigations of the ionosphere. *Radio Sci.*, *52*, 305–320. doi: 10.1002/2016RS006186

Greenwood, R. I., Parkinson, M. L., Dyson, P. L., & Schulz, E. W. (2011). Dominant ocean wave direction measurements using the TIGER SuperDARN systems. *J. Atmos. Sol.-Terr. Phys.*, *73*, 2379–2385. doi: 10.1016/j.jastp.2011.08.006

He, L.-S., Dyson, P. L., Parkinson, M. L., & Wan, W. (2004). Studies of medium scale travelling ionospheric disturbances using TIGER SuperDARN radar sea echo observations. *Ann. Geophys.*, *22*, 4077–4088. doi: 10.5194/angeo-22-4077-2004

Hosokawa, K., Iyemori, T., Yukimatu, A. S., & Sato, N. (2000). Characteristics of solar flare effect in the high-latitude ionosphere as observed by the SuperDARN radars. *Adv. Polar Upper Atmos. Res.*, *14*, 66–75. doi: 10.15094/00006304

Hosokawa, K., & Nishitani, N. (2010). Plasma irregularities in the duskside subauroral ionosphere as observed with midlatitude SuperDARN radar in Hokkaido. *Radio Sci.*, *45*, RS4003. doi: 10.1029/2009RS004244

Koustov, A. V., Sofko, G. J., André, D., Danskin, D. W., & Benkevitch, L. V. (2004). Seasonal variation of HF radar F region echo occurrence in the midnight sector. *J. Geophys. Res.*, *109*, A06305. doi: 10.1029/2003JA010337

Koustov, A. V., Ullrich, S., Ponomarenko, P. V., Nishitani, N., Marcucci, F. M., & Bristow, W. A. (2019). Occurrence of F region echoes for the polar cap SuperDARN radars. *Earth Planet Sp*, *71*, 112. doi: 10.1186/s40623-019-1092-9

Liu, E. X., Hu, H. Q., Liu, R. Y., Wu, Z. S., & Lester, M. (2012). An adjusted location model for SuperDARN backscatter echoes. *Ann. Geophys.*, *30*, 1769–1779. doi: 10.5194/angeo-30-1769-2012

Makarevich, R. A. (2010). On the occurrence of high-velocity E-region echoes in SuperDARN observations. *J. Geophys. Res.*, *115*, A07302. doi: 10.1029/2009JA014698

Marcucci, M. F., Coco, I., Massetti, S., Pignalberi, A., Forsythe, V., Pezzopane, M., ... Salvati, A. (2021). Echo occurrence in the southern polar ionosphere for the SuperDARN Dome C East and Dome C North radars. *Polar Sci.*, *28*, 100684. doi: 10.1016/j.polar.2021.100684

McDonald, A. J., Whittington, J., de Larquier, S., Custovic, E., Kane, T. A., & Devlin, J. (2013). Elevation angle-of-arrival determination for a standard and a modified SuperDARN HF radar layout. *Radio Sci.*, *48*, 709–721. doi: 10.1002/2013RS005157

Milan, S. E., Jones, T. B., Robinson, T. R., Thomas, E. C., & Yeoman, T. K. (1997). Interferometric evidence for the observation of ground backscatter originating behind the CUTLASS coherent HF radars. *Ann. Geophys.*, *15*, 29–39. doi: 10.1007/s00585-997-0029-y

Nishitani, N., & Ogawa, T. (2005). Model calculations of possible ionospheric backscatter echo area for a mid-latitude HF radar. *Adv. Polar Upper Atmos. Res.*, *19*, 55–62.

Nishitani, N., Ruohoniemi, J. M., Lester, M., Baker, J. B. H., Koustov, A. V., Shepherd, S. G., ... Kikuchi, T. (2019). Review of the accomplishments of mid-latitude Super Dual Auroral Radar Network (SuperDARN) HF radars. *Prog Earth Planet Sci*, *6:27*. doi: 10.1186/s40645-019-0270-5

Oinats, A. V., Nishitani, N., Ponomarenko, P., & Ratovsky, K. G. (2016). Diurnal and seasonal behavior of the Hokkaido East SuperDARN ground backscatter: simulation and observation. *Earth Planet Sp*, *68:18*. doi: 10.1186/s40623-015-0378-9

Ponomarenko, P. V., St. Maurice, J.-P., Hussey, G. C., & Koustov, A. V. (2010). HF ground scatter from the polar cap: Ionospheric propagation and ground surface effects. *J. Geophys. Res.*, *115*, A10310. doi: 10.1029/2010JA015828

Ribeiro, A. J., Ruohoniemi, J. M., Baker, J. B. H., Clausen, L. B. N., Greenwald, R. A., & Lester, M. (2012). A survey of plasma irregularities as seen by the midlatitude Blackstone SuperDARN radar. *J. Geophys. Res.*, *117*, A02311. doi: 10.1029/2011JA017207

Ribeiro, A. J., Ruohoniemi, J. M., Baker, J. B. H., N., C. L. B., de Larquier, S., & Greenwald, R. A. (2011). A new approach for identifying ionospheric backscatter in midlatitude SuperDARN HF radar observations. *Radio Sci.*, *46*, RS4011. doi: 10.1029/2011RS004676

Ruohoniemi, J. M., & Greenwald, R. A. (1997). Rates of scattering occurrence in routine HF radar observations during solar cycle maximum. *Radio Sci.*, *32*(3), 1051–1070. doi: 10.1029/97RS00116

Shand, B. A., Milan, S. E., Yeoman, T. K., Chapman, P. J., Wright, D. M., Jones, T. B., & Pederson, L. T. (1998). CUTLASS HF radar observations of the Odden ice tongue. *Ann. Geophys.*, *16*, 280–282. doi: 10.1007/s00585-997-0063-9

Shepherd, S. G. (2014). Altitude-adjusted corrected geomagnetic coordinates: Definition and functional approximations. *J. Geophys. Res. Space Physics*, *119*, 7501–7521. doi: 10.1002/2014JA020264

Shepherd, S. G. (2017). Elevation angle determination for SuperDARN HF radar layouts. *Radio Sci.*, *52*, 938–950. doi: 10.1002/2017RS006348

Shepherd, S. G., Sterne, K. T., Thomas, E. G., Ruohoniemi, J. M., Baker, J. B. H., Parris, R. T., ... Holmes, J. M. (2020). Bistatic observations with SuperDARN HF radars: First results. *Radio Sci.*, *55*. doi: 10.1029/2020RS007121

Tapping, K. F. (2013). The 10.7 cm solar radio flux ($F_{10.7}$). *Space Weather*, *11*, 394–406. doi: doi:10.1002/swe.20064

Thomas, E. G., Shepherd, S. G., Sterne, K. T., Kotyk, K., Schmidt, M., Bland, E. C., ... Burrell, A. G. (2020). *SuperDARN Radar Software Toolkit (RST) 4.3.1* [Software]. Zenodo. doi: 10.5281/zenodo.3634732

Titheridge, J. E. (2000). Modelling the peak of the ionospheric E-layer. *J. Atmos.*

Sol. Terr. Phys., *62*, 93–114. doi: 10.1016/S1364-6826(99)00102-9

Wang, W., Zhang, J. J., Wang, C., Nishitani, N., Yan, J. Y., Lan, A. L., ... Qui, H. B. (2022). Statistical characteristics of mid-latitude ionospheric irregularities at geomagnetic quiet time: Observations from the Jiamusi and Hokkaido East SuperDARN HF radars. *J. Geophys. Res. Space Physics*, *127*, e2021JA029502. doi: 10.1029/2021JA029502

Yakymenko, K. N., Koustov, A. V., & Nishitani, N. (2015). Statistical study of mid-latitude E region echoes observed by the Hokkaido SuperDARN HF radar. *J. Geophys. Res. Space Physics*, *120*, 9959–9976. doi: 10.1002/2015JA021685

Yeoman, T. K., Chisham, G., Baddeley, L. J., Dhillon, R. S., Karhunen, T. J. T., Robinson, T. R., ... Wright, D. M. (2008). Mapping ionospheric backscatter measured by the SuperDARN HF radars – Part 2: Assessing SuperDARN virtual height models. *Ann. Geophys.*, *26*, 843–852. doi: 10.5194/angeo-26-843-2008

Yeoman, T. K., Wright, D. M., Stocker, A. J., & Jones, T. B. (2001). An evaluation of range accuracy in the Super Dual Auroral Radar Network over-the-horizon HF radar systems. *Radio Sci.*, *36*(4), 801–813. doi: 10.1029/2000RS002558

Yukimatu, A. S., & Tsutsumi, M. (2002). A new SuperDARN meteor wind measurement: Raw time series analysis method and its application to mesopause region dynamics. *Geophys. Res. Lett.*, *29*, 1981. doi: 10.1029/2002GL015210

AGU PUBLICATIONS

Radio Science

Supporting Information for

Virtual height characteristics of ionospheric and ground scatter observed by mid-latitude SuperDARN HF radars

E. G. Thomas[1] and S. G. Shepherd[1]

[1]Thayer School of Engineering, Dartmouth College, Hanover, New Hampshire, USA

Contents of this file

Figures S1 to S6

Introduction

This supporting information provides a matching set of figures for the Christmas Valley West (CVW) SuperDARN radar (Figures S1-S6).

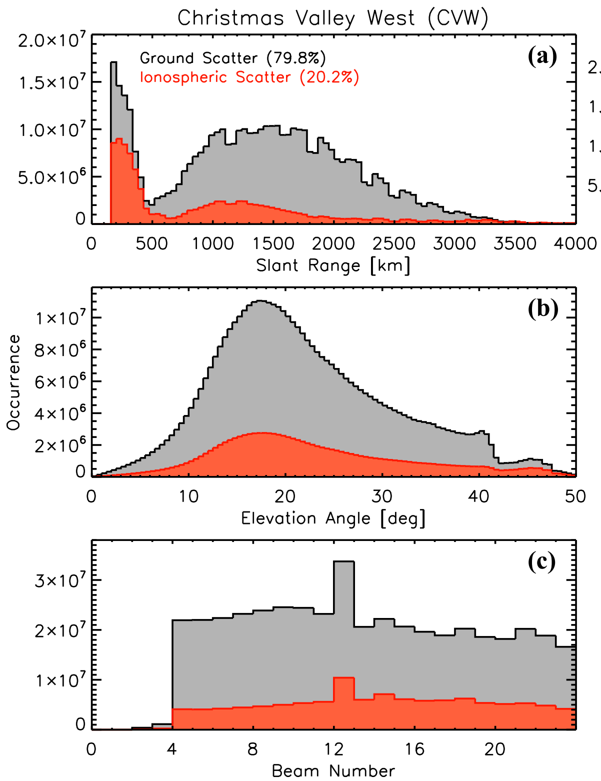

Figure S1. Statistical occurrence of Christmas Valley West (CVW) radar observations from 2014–2018 with (a) slant range, (b) elevation angle, (c) azimuthal beam number, (d) frequency, (e) Universal Time, and (f) month, sorted by ionospheric scatter (red) and ground scatter (black). Approximate local times at 6 hr intervals are indicated on panel (e) by vertical dashed lines, and the total number of measurements is given above panel (d).

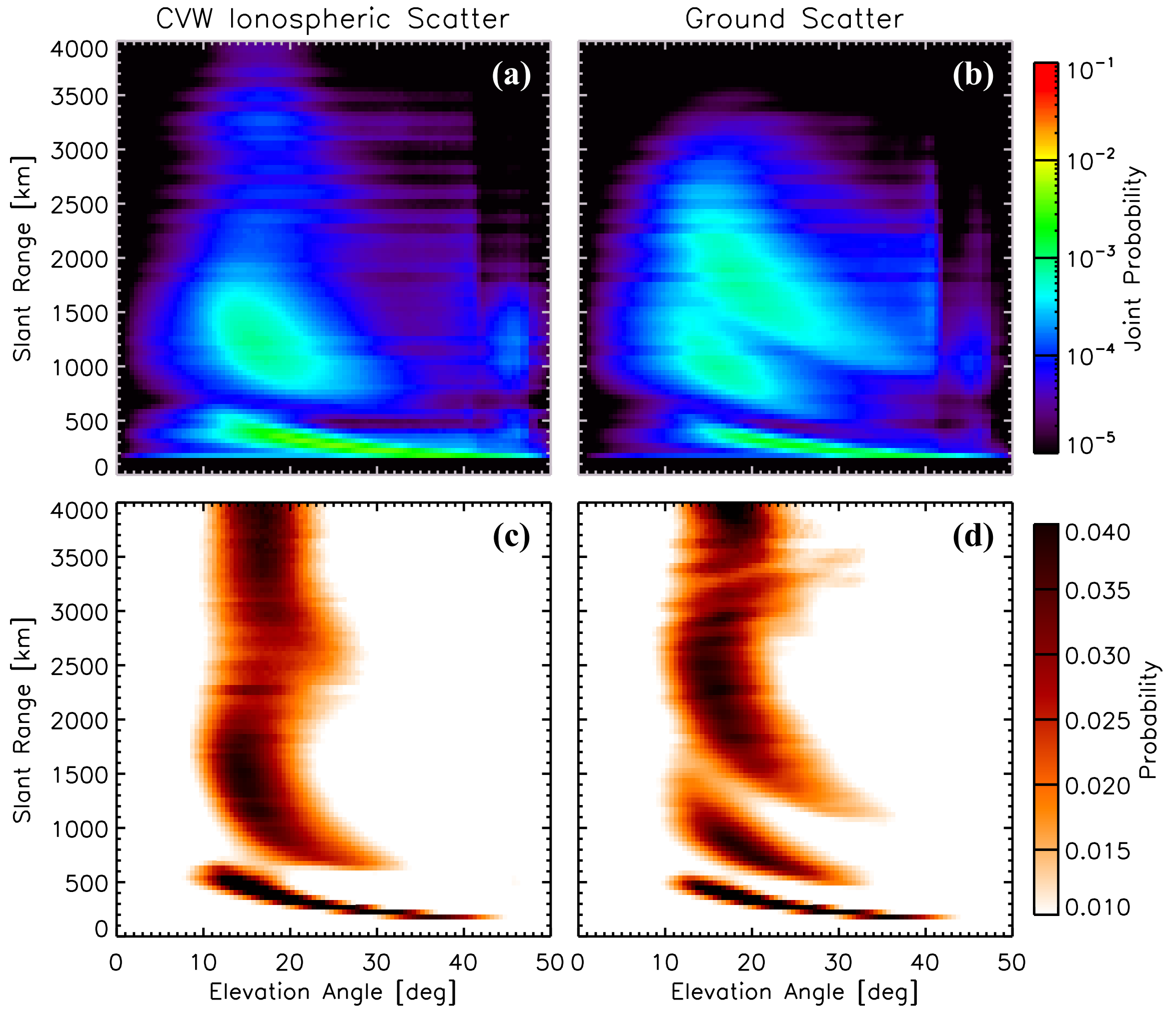

Figure S2. (top) Joint probability distributions of elevation angle and slant range observed by the CVW radar for (a) ionospheric and (b) ground scatter, in 0.5° elevation and 45 km range bins. (bottom) The same probability distributions normalized by the maximum occurrence in each range bin; occurrence probabilities of less than 0.010 are not shown.

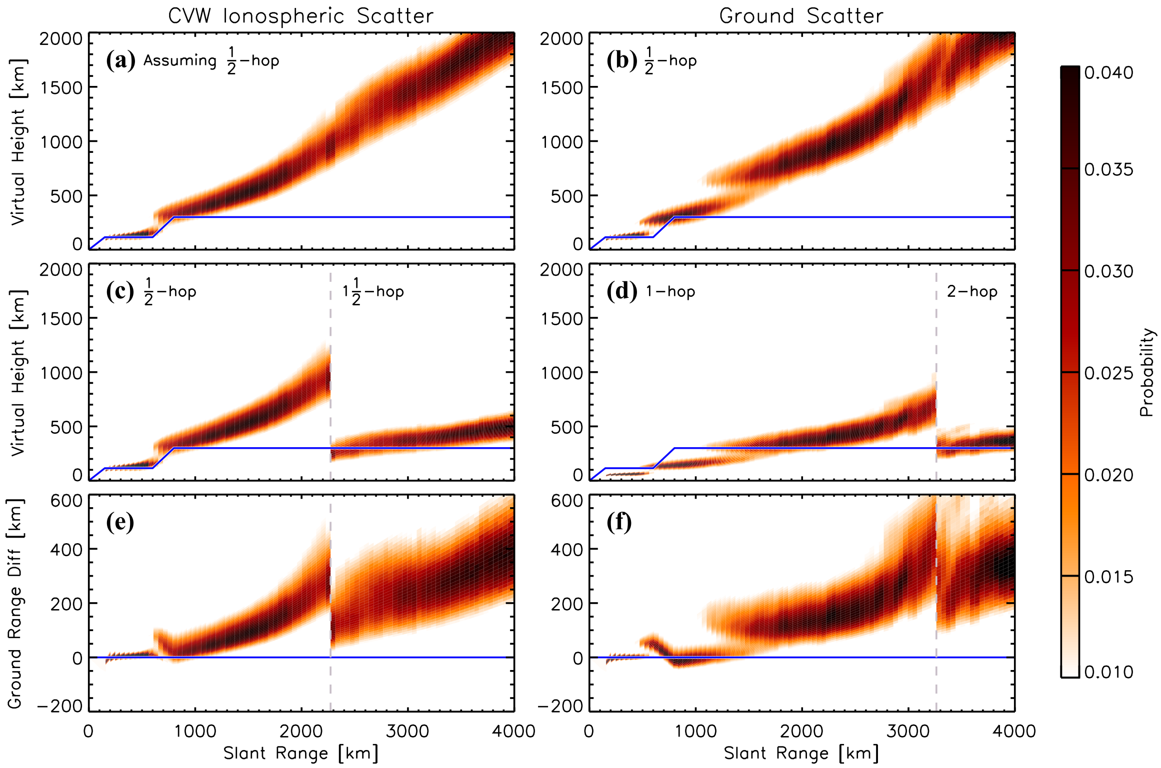

Figure S3. Normalized probability distribution of elevation angle and slant range observed by the CVW radar for (a) ionospheric and (b) ground scatter from Figure S2 mapped to slant range versus virtual height assuming a $\frac{1}{2}$-hop propagation path, with the standard virtual height model overlaid in blue. (c) Same probability distribution for ionospheric scatter as panel (a) but assuming a $1\frac{1}{2}$-hop propagation mode for slant ranges beyond 2250 km (vertical dashed line). (d) Same probability distribution for ground scatter as panel (b) but assuming a 1-hop propagation mode for slant ranges less than 3240 km (vertical dashed line) and a 2-hop propagation mode for further ranges. The bottom row shows the difference in ground ranges for (e) ionospheric and (f) ground scatter from panels (c) and (d) compared to application of the standard virtual height model (which always assumes a $\frac{1}{2}$-hop propagation path); positive values indicate the true ground range is closer to the radar than suggested by the model.

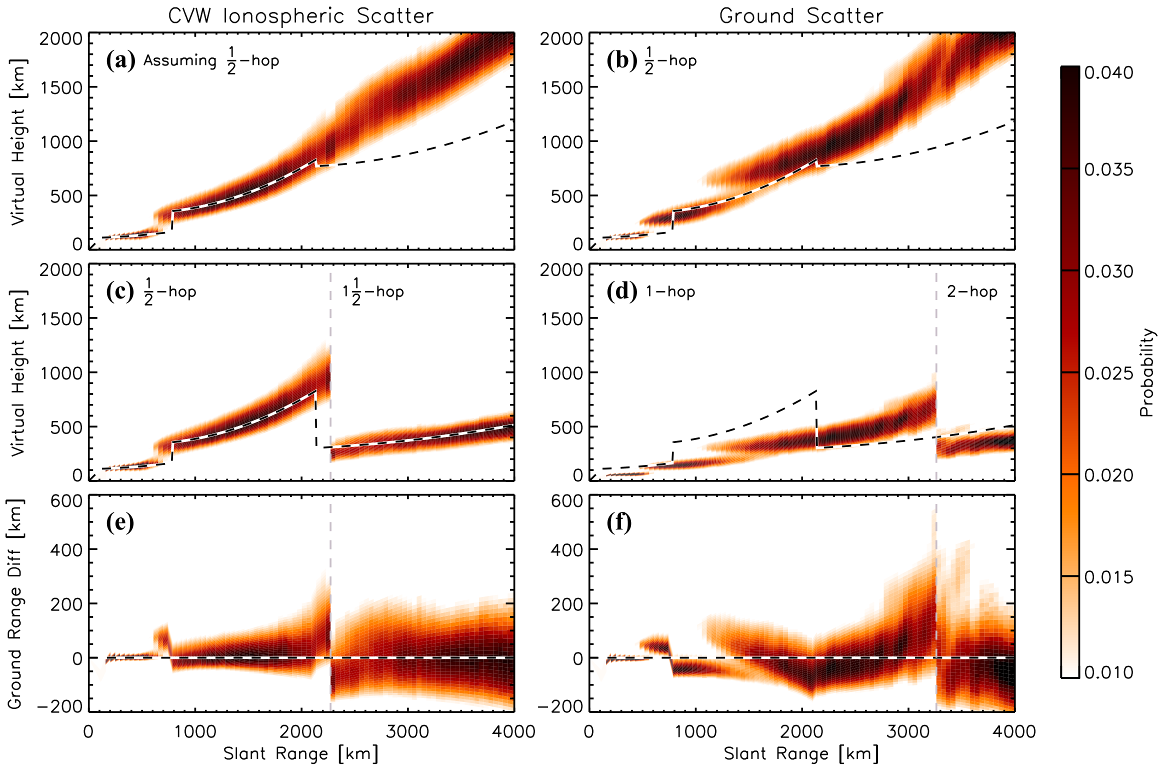

Figure S4. Normalized probability distributions of slant range and virtual height observed by the CVW radar for (left) ionospheric and (right) ground scatter in the same format as Figure S3, but instead compared against the Chisham virtual height model overlaid as a black and white dashed line. The "pseudo" virtual height predicted by the Chisham virtual height model for $1\frac{1}{2}$-hop scatter (beyond 2137 km slant range) is overlaid on panels (a–b), while the "true" virtual height predicted by the model for $1\frac{1}{2}$-hop scatter is overlaid on panels (c–d); see text for details. The bottom row shows the difference in ground ranges for (e) ionospheric and (f) ground scatter from panels (c) and (d) compared to application of the Chisham virtual height model (which assumes either a $\frac{1}{2}$-hop or $1\frac{1}{2}$-hop propagation path); positive values indicate the true ground range is closer to the radar than suggested by the model.

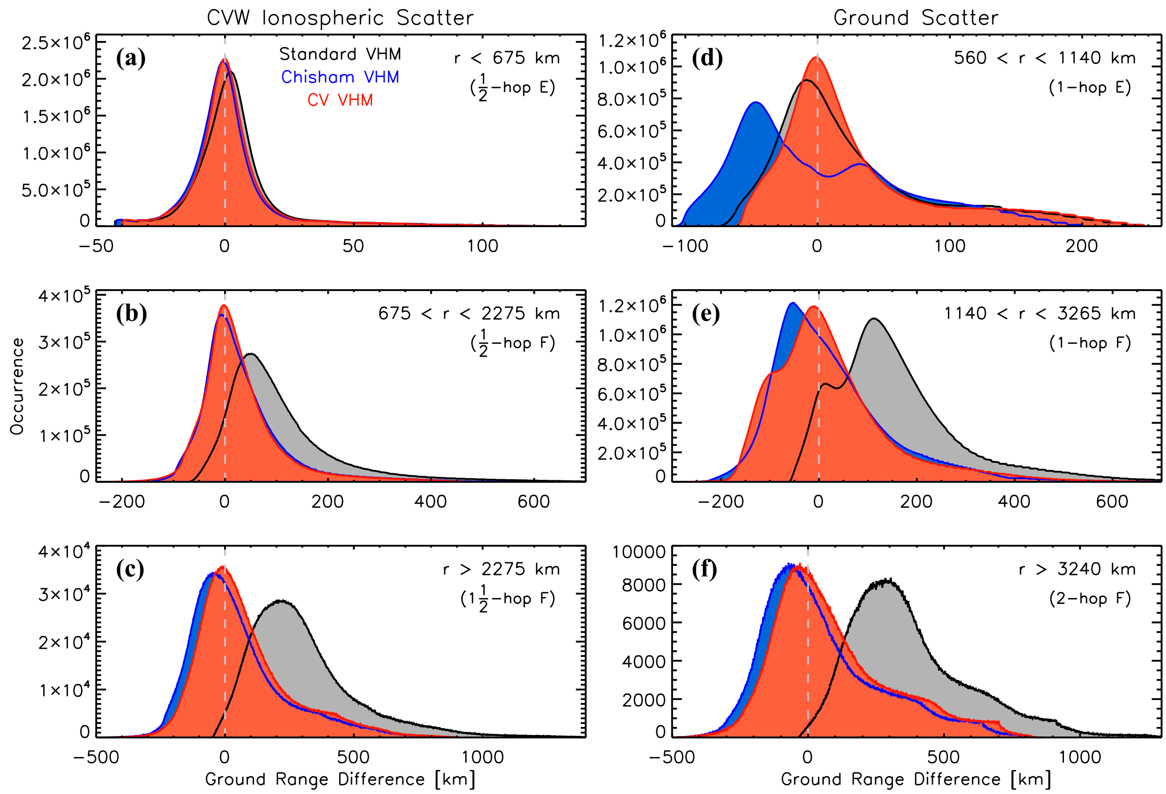

Figure S5. Differences in ground range when using the slant range and virtual height observed by the CVW radar for (left) ionospheric and (right) ground scatter compared to the standard (gray), Chisham (blue) and CV (red) virtual height models. Results are organized by (a) $\frac{1}{2}$-hop E-region, (b) $\frac{1}{2}$-hop F-region, (c) $1\frac{1}{2}$-hop F-region, (d) 1-hop E-region, (e) 1-hop F-region, and (f) 2-hop F-region scatter distributions.

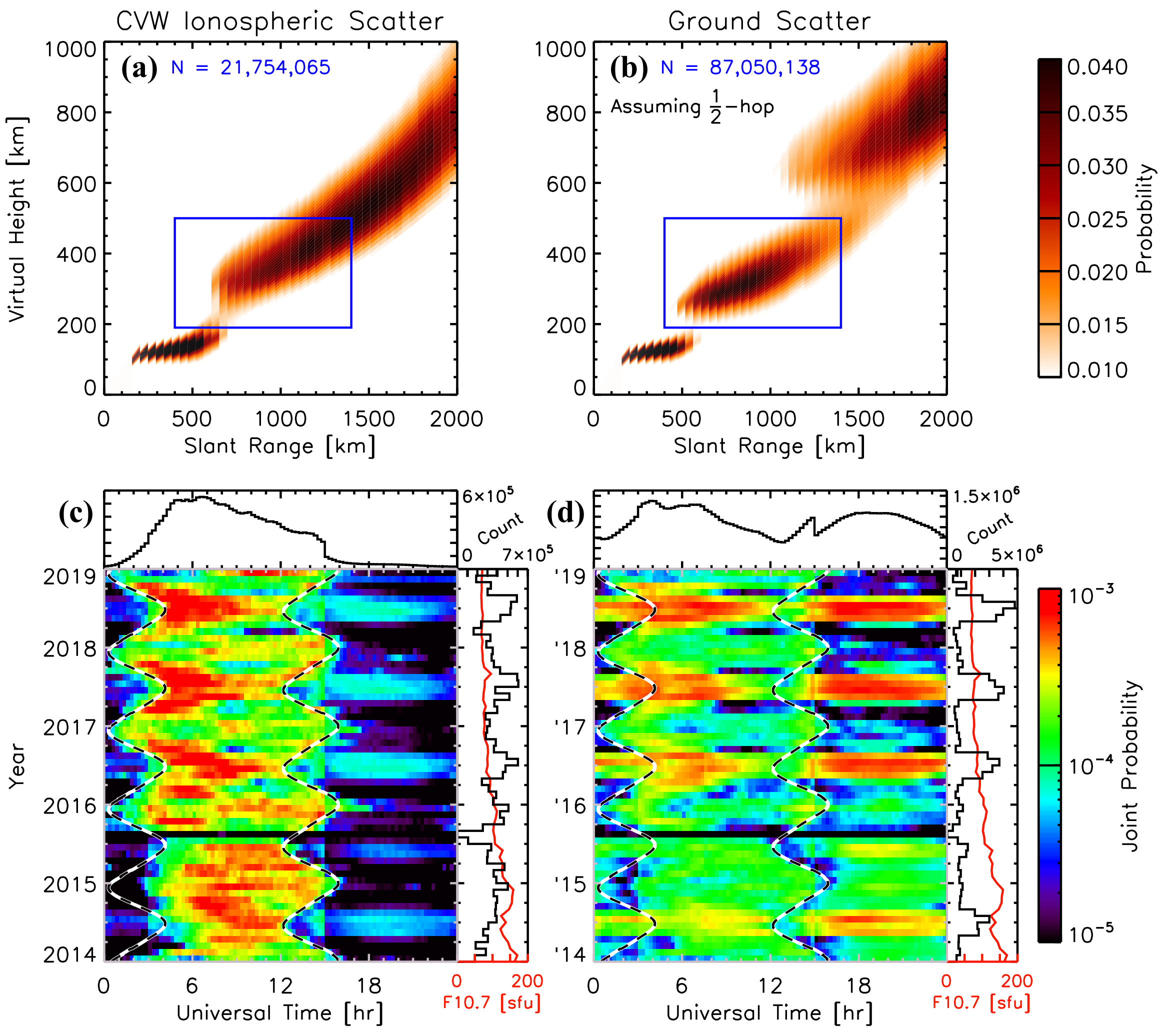

Figure S6. Normalized probability distributions of slant range and virtual height observed by the CVW radar for (a) ionospheric scatter and (b) ground scatter, centered on the region of possible "mixed" scatter indicated by the blue box. Both the ionospheric and ground scatter-flagged data in panels (a–b) have been mapped to virtual height assuming a $\frac{1}{2}$-hop propagation mode for easier comparison, and the number of observations falling within the "mixed" scatter region are given at the top of each panel in blue. (c) Joint probability distribution of Universal Time (UT) and month/year for the ionospheric-flagged scatter within the blue box in panel (a); along the top of the panel is a 1-D histogram of the same data as a function of UT only, while along the right side of the panel is a 1-D histogram as a function of month and year with the monthly average F10.7 solar radio flux overlaid in red. (d) Same as panel (c) but for the ground scatter-flagged data within the blue box in panel (b). Approximate sunrise and sunset times at the midpoint between the CVW radar and "mixed" scatter backscattering volume are overlaid on panels (c–d) as black and white dashed lines.